MASTER THESIS

Development of an Underwater 3D LED Multispectral Imaging System

Supervisors:
Prof. Dr.-Ing. Udo Frese
Dr. Jakob Schwendner

Author:
Fabian Hauschildt

May 23, 2021

Urheberrechtliche Erklärung

Hiermit versichere ich, dass ich meine Abschlussarbeit ohne fremde Hilfe angefertigt habe und dass ich keine anderen als die von mir angegebenen Quellen und Hilfsmittel benutzt habe.

Alle Stellen, die wörtlich oder sinngemäs aus Veröffentlichungen entnommen sind, habe ich unter Angabe der Quellen als solche kenntlich gemacht.

Die Abschlussarbeit darf nach Abgabe nicht mehr verändert werden.

Datum: —————————— Unterschrift: ——————————————

Erklärung zur Veröffentlichung von Abschlussarbeiten

☐ Ich bin damit einverstanden, dass meine Abschlussarbeit im Universitätsarchiv für wissenschaftliche Zwecke von Dritten eingesehen werden darf.

☐ Ich bin damit einverstanden, dass meine Abschlussarbeit nach 30 Jahren (gem. §7 Abs. 2 BremArchivG) im Universitätsarchiv für wissenschaftliche Zwecke von Dritten eingesehen werden darf.

☐ Ich bin *nicht* damit einverstanden, dass meine Abschlussarbeit im Universitätsarchiv für wissenschaftliche Zwecke von Dritten eingesehen werden darf.

Datum: —————————— Unterschrift: ——————————————

Contents

List of Figures

List of Tables

Chapter 1

Introduction and Motivation

1.1 Motivation

Intentionally, conventional imaging is answering the question *"Where?"*. 3D imaging is adding a third dimension to the spatial information in images, resulting in a more detailed answer to that question. Analog to this, classical spectroscopy is answering the question *"What?"*. Multispectral imaging is adding spectral information to images. Consequently, 3D multispectral imaging answers the question of *"Where is what in the 3D space?"*. This alone is already an interesting question, but providing an answer for this in the underwater world opens a new window of opportunities. Underwater imaging takes place in a harsh environment. The light, which is essential for imaging, undergoes absorption that depends on the composition of the water. This effect is distorting the colors in underwater images. The impact of this phenomenon increases significantly with the distance of scene points to the camera. Color correction in underwater images is thus a nontrivial task and becomes even more difficult for scenes which are not flat because the distance of a scene point is often unknown. The 3D information in this environment is very valuable and the potential of this information for spectral imaging underwater is great. Just as conventional imaging, spectral imaging measures the reflected light from the scene. Knowing how far photons had to travel from the light source to the sensor, would allow an accurate correction of the spectral measurement if the absorption coefficient is known. If not, the gathered information can be used to determine it. An accurate spectral 3D image has many potential use cases in fields like archaeology [22], geology [24], biology [25], industrial inspection, and basically every operation that is based on a detailed visual inspection because it adds valuable information to answer the *"What?"* question. For example, a in situ coral health analysis on spectral data was performed by [18].

Usually, multispectral imaging systems are multi-band filter systems, which are associated with high costs. The recent evolution of high-power narrowband LEDs leads to a new way of building multispectral imaging systems [35]. LED-based multispectral imaging systems can be very fast and are usually space and cost efficient. In addition, these LED-based systems are energy-efficient because the light is not necessarily filtered. This is particularly relevant for battery-powered systems. This work will take advantage of the recent developments and in its context an underwater multispectral 3D imaging system based on multiple LED illuminations will be built.

1.2 Introduction

This work is done in cooperation with the Kraken Robotik GmbH (KRG) Bremen. The Company is focused on the development of underwater vision systems that are used on underwater water vehicles. KRGs core product is a 3D underwater scanner system, that can obtain detailed spatial

information of a scene. Within the framework of this work, a multi-band LED light source was developed. In combination with a 3D scanner system it forms a 3D underwater multispectral imaging system. The reader will first be introduced to the topic of spectral imaging, before recent work in the field of LED multispectral imaging will be presented. Afterwards, the main parts of the interdisciplinary development task are going to be depicted. The raw multispectral data acquired by the developed system will be used to experimentally find a suitable spectral estimation method. And finally, the system will be tested in a laboratory environment.

The objective of this thesis is to obtain a Master's degree in Systems Engineering from the University of Bremen.

Chapter 2

Hyper- and Multispectral Imaging

Here, the reader is introduced to the topic of spectral imaging. First of all, some fundamentals on spectra, reflectance, and water properties are provided. The concepts of hyper- and multispectral imaging and how to distinguish them are as well presented. Then an insight into the theory and state of the art of LED multispectral imaging is given. Finally, the concept of spectral estimation from multispectral data is introduced with an overview of selected methods.

2.1 Fundamentals

2.1.1 Properties of Light

In 1666 Isaac Newton was the first known scientist to break the sunlight in its components using a prism of glass in a dark room with only one hole for the sunlight to shine in [32]. He was the first one to call the resulting color gradient a spectrum and he concluded that all colors are made by light and are either spectral colors or compounded of these [14].

Much later, in the nineteenth century, it was found that light is an electromagnetic wave characterized by speed v, wavelength λ, and frequency f as in the following equation [9]:

$$v = f\lambda \tag{2.1}$$

A small sector of the electromagnetic spectrum which includes the human perceptible wavelengths is shown in figure 2.1. It shows the color, most humans see when their eyes are stimulated by light with the corresponding wavelength. To wavelengths below 300 nm and above 700 nm the human eye has no sensitivity. Light in this range is called ultraviolet or respectively infrared.
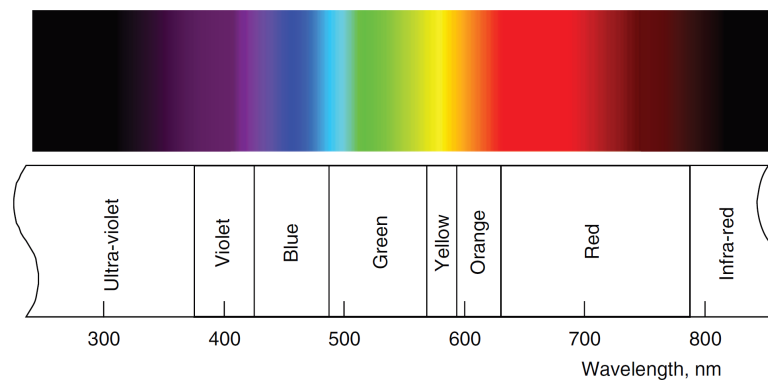
Figure 2.1: A section of the electromagnetic spectrum containing the visible wavelengths and the usual color names assigned to it. Source: [32]

In the twentieth century during the development of quantum theory, the particle-like behavior of light in experiments was explained by a stream of light quanta that carry a certain amount of energy. These quanta are called photons. The energy E of one photon was described by Max Planck with the following relation [9]:

$$E = hf \tag{2.2}$$

The photon's energy is proportional to the electromagnetic wave's frequency with the Planck constant h. With equation 2.1 it can be seen that the energy increases with smaller wavelengths in the electromagnetic spectrum.

2.1.2 Human Color Perception

The reason why we as humans are able to distinguish about 10 million colors is closely related to the principle of color imaging and thus also spectral imaging. Because of this, the human color perception will be presented here in a descriptive manner. All information for this is taken from [32], where a deeper insight into this topic is provided.

Similar to light path in the technical components of a camera, the light of a scene passes the optical components of the eye. The light travels through the cornea, pupil ,and lens, while the iris acts as an aperture. This results in a rotated picture of the scene on the retina. The retina contains different receptors that are connected to the nervous system. These receptors can be divided into two types, the rods, and the cones. Their sensitivity to light is presented in figure 2.2.
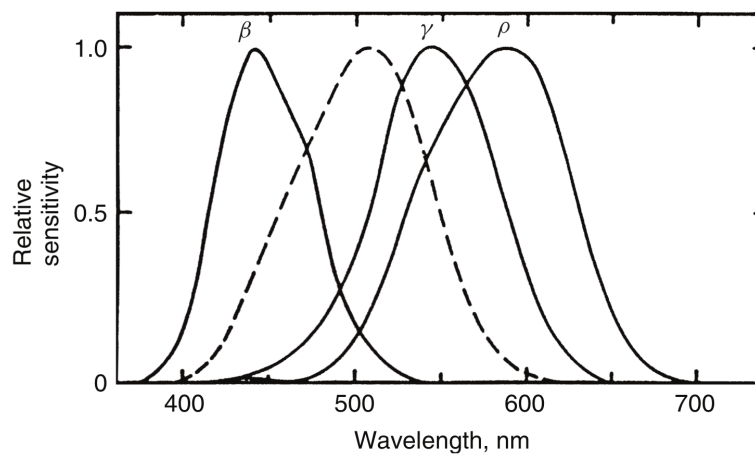
Figure 2.2: Normalized spectral sensitivities of the human retina. Broken line: Sensitivity of the scotopic vision made by rods. β, γ, ρ: Sensitivity of the photopic vision caused by the three different types of cones. Source: [32]

The rods are responsible for vision under conditions with low light intensity. They are responsible for what is called scotopic vision. Considering the spectral sensitivity of the scotopic vision, see the broken line in figure 2.2, it becomes plausible that we see dark scenes in a blue to green color. But if our visual perception solely consisted of scotopic vision, humans would not be able to distinguish colors at all. This can be illustrated by imagining the stimulus of the scotopic vision to monochrome light of different wavelengths. Light with a certain intensity and a wavelength of 500 nm results in the same stimulus as light with a wavelength of 550 nm and 3 times the intensity. Consequently, it is not possible to extract information about the light's wavelength out of resulted stimulus. It is the same as in a monochromatic camera. Thus, the cones are indispensable for color vision. They are responsible for vision under brighter conditions where the rods become less important. This cone-based vision is called photopic vision. Because of different pigments

in the cones, they are active in different areas of the spectrum and can be divided into the types ρ, γ, β which correspond to the RGB color space. Now, with incident light of different colors, the relation of the stimuli from the different cone types changes. This relation in combination with the stimuli intensity can be interpreted by the brain to make color perception possible. With the sensitivities of the cones, figure 2.2 also shows why we are only able to see the range of 400-700 nm of the electromagnetic spectrum.

2.1.3 Light-Matter Interaction

The basis for spectral imaging is given by the physical and chemical properties of matter which determine its interaction with light. Photons emitted by any light source have a certain energy and trajectory which both will be affected by the illuminated sample [3]:

The energy will decrease mostly depending on the chemical properties of the sample's molecules and the trajectory is influenced by its reflection. The basic effects that can occur in the path of a photon from the source to a detector are absorption, reflection, and transmission. These are depicted in figure 2.3.
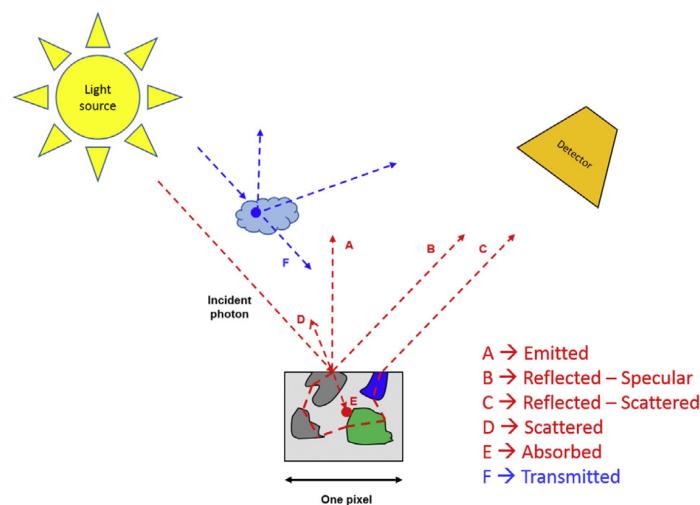
Figure 2.3: Depiction of possible light-matter interactions when photons hit a sample. Source: [3]

According to [3], absorption occurs when the frequency of a photon that hits the molecules of a sample is the vibrational frequency of its electrons. Consequently, the energy is passed to the sample and cannot reach the detector, see E in figure 2.3.

If the frequencies do not match as in the absorption case, the photon is either transmitted or reflected. This is depending on the wavelength, molecule properties, surface characteristics,

and angle of the incident photon. As depicted in figure 2.3, a photon can be reflected specular or scattered. In the case of scattering the reflection of the light source becomes diffuse and scattered photons do not necessarily hit the detector, see example D in figure 2.3. It is also possible, that the photon is at first transmitted but then reflected from the interior of the sample. For example, human veins can become visible to a detector under near-infrared light [3]. This is also an example of how spectral imaging can be used, to analyze structures that are naturally not perceptible to humans.

As presented in section 2.1.1 colors are based on the perception of light. We can detect light that is somehow reflected from an object. The color arriving at the detector is strongly, but not exclusively influenced by the incident light. Equally important is the wavelength-dependent spectral reflectance at a given point on that object's surface $r(\lambda)$. If the spectral radiance of the illuminant is given by the function $l(\lambda)$, the radiance of the light being reflected from the object $f(\lambda)$ can be modeled with equation 2.3 [14].

$$f(\lambda) = l(\lambda)r(\lambda) \tag{2.3}$$

The spectral reflectance has always a magnitude between 0 and 1. Consequently, it can be interpreted as a probability, if a photon with a certain energy is reflected by the sample [16]. Spectral imaging measures the spectral reflectance in combination with spatial information of the scene. The model in equation 2.3 is limited. It is not considering the geometry of the scene and the spectral reflectance may depend on the angles of the incident light and the observation [14]. Usually, the spatial information in spectral images is 2D and thus the implementation of a model that is considering the scene's surface angles with respect to the observer and illuminant is not feasible. In this work however the spatial information will be 3D and the geometrical information from the scene will later be used to perform a more accurate reconstruction of the spectral reflectance factor. More complex reflection behavior can be described by spectral bidirectional reflectance distribution functions [14]. Out of simplicity, here only diffuse reflection independent from material properties will be considered with Lambertian reflectance. This is defined as follows: "Lambertian reflectance is a scene property that distributes the energy from any incident illumination into all viewing directions equally." [21]. A measurement of Lambertian reflection in one point of the scene can be described by the following equation [21]:

$$E = I\rho max(\mathbf{n} \cdot \mathbf{s}, 0) \tag{2.4}$$

E denotes the measured intensity of the reflected light from the Lambertian surface with the normal vector $\mathbf{n}$. I is the incident light intensity, its direction is described by the vector $\mathbf{s}$ and ρ is a factor, that describes the ratio of the reflected and incident energies for that scene point. The dot product relation between the incident light direction and the surface normal vector is plausible because the scene area illuminated by the incident light becomes larger with a cosine relation.

The maximum of the dot product and zero is taken because reflections with more than 90 degrees versus the normal are not possible.

2.1.4 Metamerism

As presented in section 2.1.2 color perception is based on the cone stimuli β, γ and ρ. The continuous spectrum is compressed to three values, from which a perfect recovery of the spectral distribution is not possible. This implies that stimuli can be the same despite a different spectral distribution of the light. This phenomenon is referred to as metamerism and the colors are then called metameric [32]. An example of this phenomenon can be seen in figure 2.4: The spectral power distributions N and S are completely different, but the areas under the cone sensitivity functions are the same. Consequently, the resulting stimuli are the same and thus their colors are indistinguishable from each other.
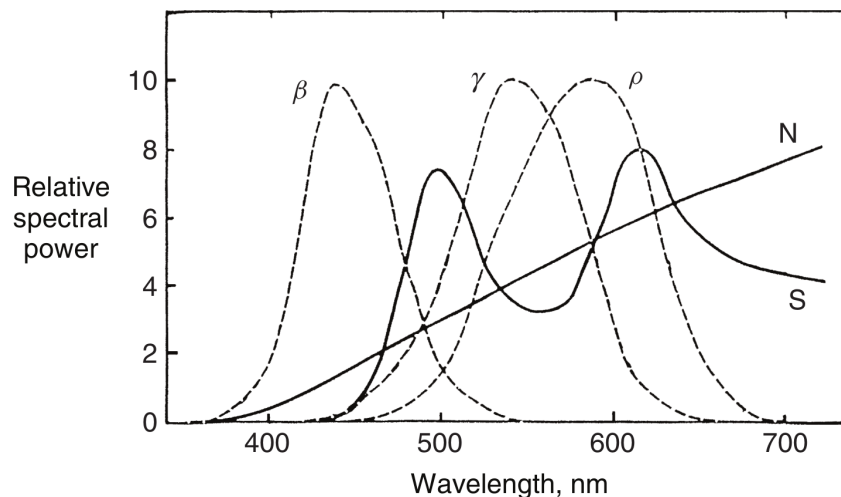
Figure 2.4: Example of metamerism. Despite a different spectral power distribution, the stimuli from N and S are the same for the different cones β, γ and ρ. Source: [32]

Usually, the metamerism of objects can be broken up by changing the light under which they are observed, because the radiance being reflected is a function of the light, see equation 2.3.
This is problematic for some fields like the textile industry which aims for color matches under different lights. But despite the problems metamerism can cause, it is an important and highly useful phenomenon for color science. Without metamerism, the only way to reconstruct colors would be to exactly match their reflectance [14]. Nevertheless, metamerism shows that classic three-channel color imaging has limits and that for an accurate analysis of the object's properties, further information about the reflectance is necessary.

2.1.5 Underwater Conditions

The system developed within the framework of this thesis will be deployed in underwater conditions. Therefore, the significant effects of the underwater environment for the imaging system are presented. The major effect water has on light is attenuation, also called absorption. It is caused by both water molecules and dissolved particles, which absorb photons. The intensity $I_d(\lambda)$ of light with a certain wavelength that traveled the distance d in a medium is described by the Beer-Lambert law [19]:

$$I_d(\lambda) = I_0(\lambda)e^{-\alpha(\lambda)d} \tag{2.5}$$

$I_0(\lambda)$ describes the initial light intensity and $\alpha(\lambda)$ is the absorption coefficient, that characterizes the medium. Because of the wavelength dependency in the absorption coefficient, the light intensity is not reduced uniformly over its spectrum, which leads to a change of the perceived light color. Because seawater contains various particles in different concentrations, the absorption coefficient is dependent on the composition of the water [19]:

$$\alpha(\lambda) = \alpha_{PP}(\lambda) + \alpha_{NAP}(\lambda) + \alpha_{CDOM}(\lambda) + \alpha_W(\lambda) \tag{2.6}$$

In the above equation the absorption coefficient is modeled with its four main contributors: Phytoplankton (PP), non-algal particles (NAP), colored dissolved organic matter (CDOM), and pure seawater (W). A model for each contribution is provided by [19]. It can be seen in figure 2.5.
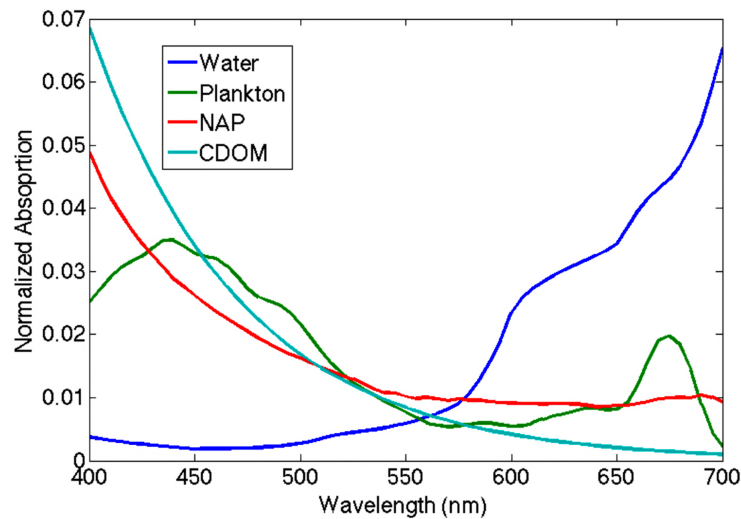
Figure 2.5: Contributions to the absorption coefficient. The curves are normalized and their magnitude depends, except for the water curve, on the corresponding particle concentration in water. Source: [19]

Another aspect of underwater imaging is backscatter [19]. It is caused by light that reaches the camera without seeing the target because it is reflected by particles in the water. For this

thesis, backscatter is less relevant because the system will be tested in clear water. Consequently, backscatter will not be seen in the data and thus cannot be evaluated.

2.2 Spectral Imaging Systems in General

2.2.1 General System Configuration

The acquisition of hyper- and multispectral images is possible with many different methods and systems. But in general, they are a mixture of conventional imaging and conventional single-point spectroscopy, so that a combination of both technologies makes the Design of hyper- and multispectral imaging systems feasible [2]. The general system configurations of conventional imaging and spectroscopy as well as the resulting combination for hyper- and multispectral are illustrated in figure 2.6.All systems contain a Light source, that is illuminating a sample.

Conventional Imaging

Light Source ⇒ Sample ⇒ Area Detector

Conventional Spectroscopy

Light Source ⇒ Sample ⇒ Wavelength Dispersion Device ⇒ □ Point Detector

Hyper- and Multispectral Imaging

Light Source ⇒ Sample ⇒ Wavelength Dispersion Device ⇒ Area Detector

Light Source ⇒ Wavelength Dispersion Device ⇒ Sample ⇒ Area Detector
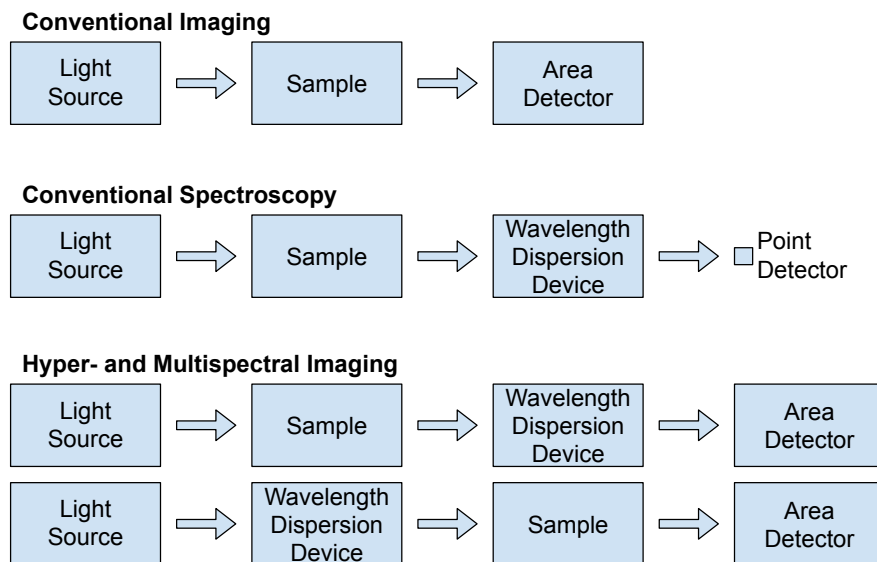
Figure 2.6: General system configurations of conventional imaging, conventional spectroscopy, and hyper- and multispectral imaging. The arrows indicate the path of the light. Sources: [29] and [3] *(modified)*

If spectral detailed information is required, the light passes a type of wavelength dispersion device like a prism or filter wheel either before or after the sample. In the end, all systems need a detector which is for all imaging systems, in general, an area detector. The connection between spectroscopy and hyperspectral imaging was described by Quin: "If conventional imaging tries to answer the question *where* and conventional spectroscopy tries to answer the question *what*, then hyperspectral imaging tries to answer the question *where is what*." [29].

2.2.2   Spectral Information in Images

The information in images is not only spatial, but also spectral and different types of images can be classified by the spectral information each pixel contains [2]:

The least spectral information is given in single-channel images. Usually, they are represented with a grayscale color map and have a high spatial resolution. The spectral information in single-channel images is compressed to one value and all color information is lost. To obtain color information from the electromagnetic spectrum, color-space images mimic human color perception. They are normally composed of 3 channels in the RGB color-space and hence can create a stimulus at the three types of cones described in section 2.1.2. More spectral information is found in multispectral images. They are composed of multiple images at specific wavelengths acquired with the help of optical filters or LEDs. Neither is the number of images that make up a multispectral image defined. Nor are the positions of the sample points in the wavelength domain specified. The sampling is discontinuous and there lies the contrast to hyperspectral images. Hyperspectral images provide a continuous measurement of the spectrum for each pixel with the spectral resolution given in nanometers. Consequently, hyperspectral images provide the highest quantity of spectral information. The described difference between hyper- and multispectral imaging is depicted in figure 2.7.
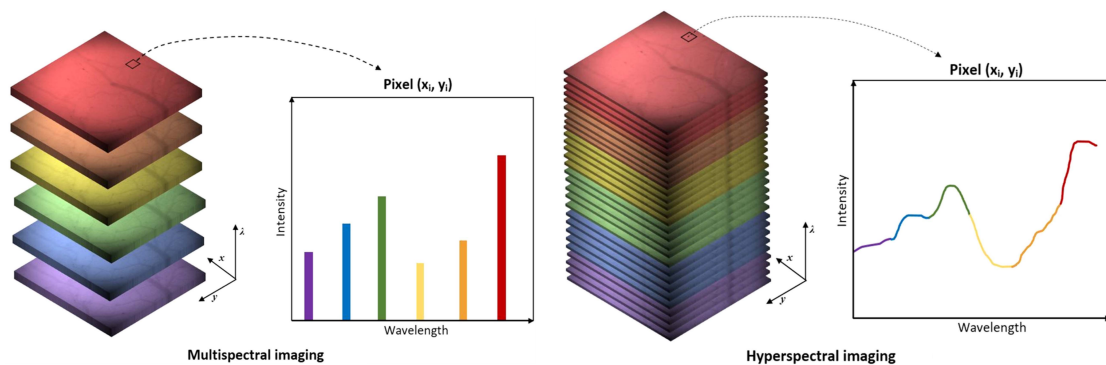
Figure 2.7: Different principles to acquire multi- or hyperspectral images. The images contain the two spatial dimensions *x* and *y* and the spectral dimension λ. Source: [12] *(modified)*

2.2.3   RGB Representation of Spectral Images

Hyperspectral images can be viewed layer by layer in grayscale or any other color mapping. This way they show only the reflection of the scene for a specific wavelength interval. This might be very interesting or inconvenient. This depends on the viewer's intention. However, it might be useful to transform the spectral information into RGB values that are commonly used for displaying colors digitally. Hyperspectral images may contain spectral information that
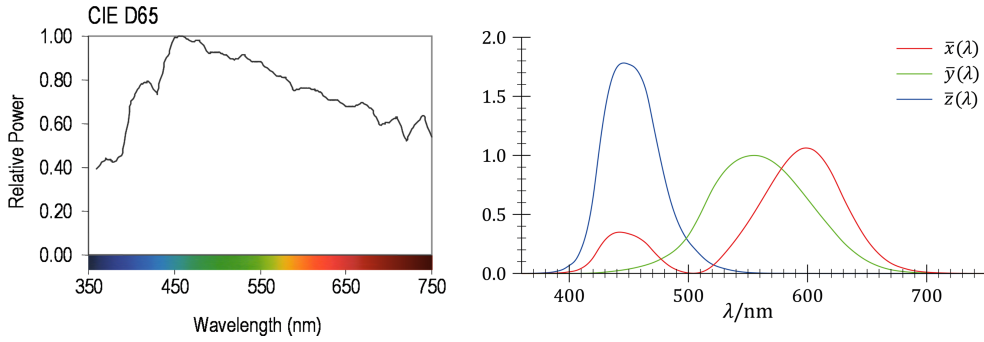
Figure 2.8: CIE Standard Illuminant D65. Source: [43] *(modified)* Right: CIE 1931 color matching functions. Source: [41]

is outside the visible spectrum. This information can be displayed in an RGB image using a false-color representation, see [42] for further information. In this work, the obtained spectral information lies in the visible range between 400 and 700 nm. Colors in this range can be represented with RGB values, which allows a good first impression of how the spectrum might look like. Consequently, this work aims for a realistic representation of the spectra. Reflectance spectra are not directly perceived. This is the reason why they first need to be illuminated by a suitable light source. A conventional light source for this the CIE Standard Illuminant D65, which represents average daylight in the visible spectrum [33]. The relative power spectrum of the illuminant can be seen left in figure 2.8. The right half of this figure shows the CIE 1931 standard observer functions. These can be used to calculate the tristimulus values XYZ from a spectral power distribution [33]:

$$X = K \int \bar{x}(\lambda)l(\lambda)r(\lambda)d\lambda \tag{2.7}$$

$$Y = K \int \bar{y}(\lambda)l(\lambda)r(\lambda)d\lambda \tag{2.8}$$

$$Z = K \int \bar{z}(\lambda)l(\lambda)r(\lambda)d\lambda \tag{2.9}$$

In these equations, $r(\lambda)$ is the reflectance spectrum and $l(\lambda)$ is the spectral power distribution of the light source, D65 in this case. $\bar{x}(\lambda), \bar{y}(\lambda)$ and $\bar{z}(\lambda)$ are the corresponding CIE 1931 color matching functions and K is a scaling factor that is chosen to make Y equal to 100. The XYZ stimuli can then be transformed to the desired RGB values.

2.2.4 Hyper- and Multispectral Image Acquisition Methods

In principle, there are four approaches to acquire hyper and multispectral images [29]: They are the point scanning, line scanning, area scanning, and single shot method as depicted in figure 2.9. The *point scanning* or Whisk Broom scanner approach practically consists of one spectrometer,
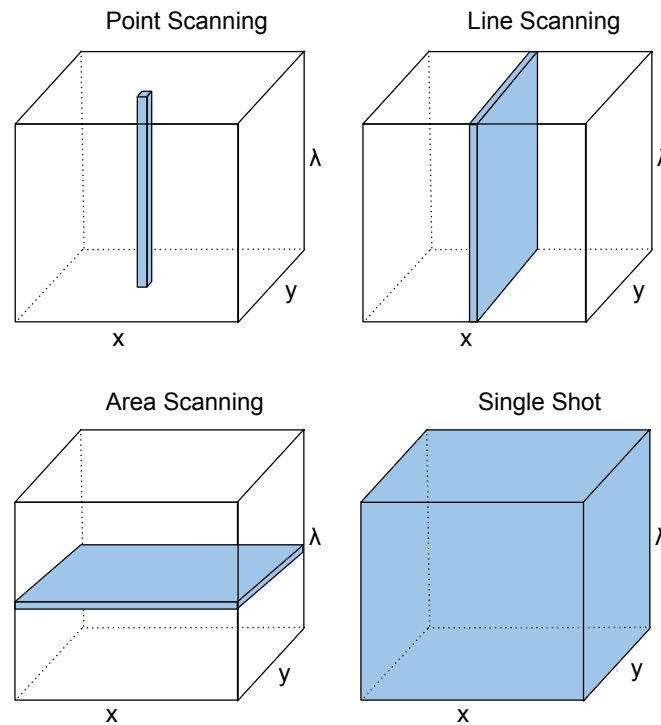
Figure 2.9: Different principles to acquire multi- or hyperspectral images. The images contain the two spatial dimensions *x* and *y* and the spectral dimension λ. Source: [29] *(modified)*

which measures only the spectral dimension. The spatial dimensions are then acquired by moving either the sample or the spectrometer [29]. This is usually a time-consuming method but it has the advantage of ensuring equal illumination for each pixel and a high spectral resolution. [3]

With the *line scanning* or Push Broom Scanner method the acquisition of 2D-spatial-spectral information is possible with each scan. The sample or measurement device must now only be moved in one direction. Consequently, the imaging process is much faster as with the Whisk Broom scanner [3].

The *area scanning* or global method makes spatial pictures of the scenes spectral information at one wavelength. Then the wavelength is changed and a new picture is taken. By stacking the images in the spectral dimension the 3D data cube can be obtained. Consequently, there is no movement of the system or target necessary. This approach is preferred for multispectral imaging systems because a smaller number of pictures can be used for the stack. It usually leads to fast and cheap systems, but it also offers less accuracy and has, depending on the wavelength dispersion device, a relatively low spectral resolution. [3]

The *single shot* method does not need any scanning in neither the spatial nor the spectral dimension. It captures the 3D data cube in one shot which makes this approach extremely fast and suitable for videos or real-time applications. But this technique is still in evolution [3].

Reasonable options for this work are the line scanning and area scanning methods, because they are of relatively low cost and the acquisition process is practicable. For the use with underwater robots, it is important, that the system works energy efficiently. Usually, operations are done in dark conditions. Consequently, all light energy is provided by battery-powered light sources. The line scanning method does not work light efficiently, because of the illuminated scene, only light for one pixel line is used for imaging. Additionally, the scene illumination has to be very bright, because the light that would illuminate one pixel line in an area scanning system is broken up and spread over a 2D sensor. Filter-based area scanning methods are also inefficient due to the light energy loss in the filters. Consequently, the best solution regarding the energy consideration is a narrow-band LED-based area scanning method, where the whole illuminated area can be imaged and no filters are needed.

2.3 LED Multispectral Imaging

2.3.1 Introduction and State of the Art

The progress in LED technology has made a large variety of narrow-band LEDs with peak wavelengths across the visual electromagnetic spectrum and beyond commercially available at low cost. They are in constant evolution, are highly efficient and have a long-life cycle [5]. LED multispectral imaging systems are in most cases implementations of the area scanning method. Multiple frames are stacked together, while each frame is illuminated differently. In contrast to filter-based area scanning systems, multiplexed LED-illumination leads to cost and energy efficient systems. The hardware setup only requires the light source, consisting of different LEDs, a controller for the light source and a camera. A broadband light source that is filtered by either expensive tunable filters or mechanically moving filter wheels is not required. This is next to the fast switching ability of LEDs one of the most substantial advantages of these systems.

Despite consisting of only three main components the LED-multispectral imaging systems built or proposed by recent research differ in their implementation. Their main differences lie in the number and selection of LEDs, if a monochromatic or a color camera sensor is used, and how the multispectral data is recorded and further processed with spectral estimation methods.

For example, Wang et al. built a multi LED-based hyperspectral imaging system with 22 different commercial LEDs [39]. Their peak wavelengths range from 440 nm to 662 nm with a maximum interval of 15 nm and they are powered with 20 mA. Their system is capable of producing hyperspectral images based on the number of samples they take in the spectral dimension.

A portable system with 23 different LEDs was built by Ramirez et al. [17]. It is measuring a much wider spectrum from 370 to 1630 nm. The system consists of two monochromatic cameras, from which one is optimized for infrared light. They also performed experiments with spectral

estimation methods, from which a Spline Interpolation achieved the best reconstruction of the reflectance spectra with their multispectral data.

A high number of different LEDs in combination with a monochromatic camera results in good accuracy, but it means that scanning in the spectral dimension needs more steps and thus more time. Consequently, the scene is constrained to be highly static. A different approach to achieve an LED-based hyperspectral imaging system was done by Tschannerl et al [37]. They used a monochromatic camera and only 3 LEDs of the colors red, green, and blue and illuminated their scene with different mixtures of these. The obtained data was then processed with a neuronal network to construct a hyperspectral image. Best results were achieved by 6 illuminations, but they lack an explanation why the additional illuminations lead to better spectral reconstruction since the scene is only illuminated by light with three different peak wavelengths.

Another method to reduce the acquisition time is to make use of the color filters in commercial cameras. Parmar et al. built a system that operates with only 5 different LED bands in the range of 400 to 700 nm [26]. They used a camera with a 3 color channel sensor. This results in 15 LED-filter combinations, from which 8 were used in further reflectance estimation. Because of noise or no gain of information 7 combinations were sorted out. For the reflectance estimation sparse methods were used.

Shretsha et al. first simulated [35] and later built [36] a LED multispectral system with a color camera, which used all filters in every image. They proposed a method to select optimal LED combinations to light the scene with 3 LEDs at once and thus reduced the number of necessary illuminations by a factor of 3. In the simulations they compared their system with 6 and nine LEDs to corresponding systems with monochrome cameras and the full number of LEDs. They compared the error of estimated reflectance spectra, which were estimated with Linear Regression. In their actual implementation 9 different LED bands with peaks between 400 and 700 nm were used within two light sources to create a uniform light distribution for the 3 illuminations. For the reconstruction of the spectrum, Wiener Estimation was used. The real system's performance was compared to the simulations, with the result that the simulations performed better, which was blamed on the difficult modeling of camera noise. Haneishi et al. designed a filter wheel based multispectral imaging system with Wiener Estimation [13]. They created a noise model and showed its influence for the Wiener Estimation.

The first application of LED multispectral imaging to underwater environments was done by Liu et al. in cooperation with the GEOMAR [23]. They used 16 high-power LEDs with 8 different bands in the visible range of the electromagnetic spectrum and a monochrome camera. They proved that most colors were better to distinguish with their multispectral setup than with RGB imaging. For this, they reduced the spectral dimensions of their images to 3 using principal component analysis. The experiment was done under controlled conditions in a water tank with 1 m distance from the camera to the color target. Thus, they were able to calibrate their system to these conditions. In addition to the first experiment, they performed also a field experiment and

showed that the acquisition of underwater multispectral images is feasible. They remarked, that the wavelength depending effect of water attenuation had to be considered in such cases, what they intended to approach by controlling the LED-channels differently.

Similar to the previous system all above LED multi- or hyperspectral setups are calibrated for a certain distance in which the light distribution is known. This way uneven illumination and disturbing camera effects are compensated. To use a LED-multispectral imaging system in less controlled environments, a solution that provides equal accuracy over all distances in the image is necessary. In this thesis, a method to solve this problem is proposed by incorporating 3D information about the scene into multispectral data processing.

2.3.2 Image Acquisition Model

As described before, LED multispectral imaging systems work with the area scanning method. The data is acquired by scanning in the spectral dimension with Q different illuminations of the scene. If a camera with P channels is used, the dimension of a single pixel measurement is $K = QP$. Mathematically the measurement can be modeled by the following equation from [36].

$$m_{pq,basic} = \int_{\Lambda} l_q(\lambda) r(\lambda) s_p(\lambda) d\lambda \tag{2.10}$$

In this equation m_{pq} denotes the camera measurement at a pixel with the pth channel with the qth illumination. $l_q(\lambda)$ is the spectral power distribution of the qth illumination and $s_p(\lambda)$ is the camera sensitivity for the pth channel. $r(\lambda)$ corresponds to the reflectance of the surface point, which is imaged by that pixel. The integration space Λ is determined by the minimal and maximal wavelength of the camera sensitivity.

This model is considering the different illuminations and camera channels, but it ignores the measurement noise, geometry, and illumination time. These effects were modeled in a multiple sensor model by [16] and can be transferred into this model in the following manner:

$$m_{pq,vacuum} = c_{pq} \int_{\Lambda} l_q(\lambda) r(\lambda) s_p(\lambda) d\lambda + n_{pq} \tag{2.11}$$

The effects of measurement geometry and illumination are modeled with the factor c_{pq} and the noise model is incorporated with the added scalar n_{pq}, which can be a complex model itself [31]. This model is valid for measurements in a vacuum and the error in air is probably negligible, but for underwater measurements, the water attenuation has to be taken into account. This is here done in the same way as in [23], by including the Beer-Lambert law into the model:

$$m_{pq,water} = c_{pq} \int_{\Lambda} l_q(\lambda) e^{-\alpha(\lambda)d_1} r(\lambda) e^{-\alpha(\lambda)d_2} s_p(\lambda) d\lambda + n_{pq} \tag{2.12}$$

$\alpha(\lambda)$ denotes the wavelength-dependent attenuation coefficient of water while d_1 and d_2 are the corresponding distances from the light source to the target surface point and from there to the

camera's water interface.

The integral of equation 2.12 can be divided into one measurement part $\phi_{pq}(\lambda)$ and one object and medium related part $o(\lambda)$:

$$\phi_{pq}(\lambda) = c_{pq}l_q(\lambda)s_p(\lambda) \tag{2.13}$$

$$o(\lambda) = r(\lambda)e^{-\alpha(\lambda)(d_1+d_2)} \tag{2.14}$$

This leads to to the following, simpler representation of equation 2.12.

$$m_{pq,water} = \int_{\Lambda} \phi_{pq}(\lambda)o(\lambda)d\lambda + n_{pq} \tag{2.15}$$

To obtain numerical solutions for this continuous equation, it needs to be discretized. A discretization of a similar equation is given in [31]. The following discretization steps are taken from there. Equation 2.15 can be written as a scalar product in matrix notation:

$$m_{pq,water} = \phi_{pq}^T o + n_{pq} \tag{2.16}$$

For this, the wavelength-dependent functions need to be sampled in N equal intervals, so that $o = [o(\lambda_1)\,o(\lambda_2)...o(\lambda_N)]^T$ and $\phi_{pq} = [\phi_{pq}(\lambda_1)\,\phi_{pq}(\lambda_2)...\phi_{pq}(\lambda_N)]^T$.

The matrix notation can now be used to represent all K measurements in one vector resulting in the following linear system:

$$m = \Phi o + n, \tag{2.17}$$

where $m = [m_{11}\,m_{12}...m_{pq}]^T$ and Φ is the $K \times N$ measurement matrix containing the sampled LED-filter combinations. The noise vector is given by $n = [n_{11}\,n_{12}...n_{pq}]^T$. For a better understanding of equation 2.17 a classical 3 color camera can be taken as an example, resulting in $K = 3$. Let the sampling be every 5 nm in the range of 400 nm to 700 nm. This makes $N = 61$ and thus Φ is a 3×61 matrix and o is a column vector with 61 entries, representing the spectrum measured by the system Φ. The result of the multiplication is a 3-dimensional column vector. Consequently, the measurement reduced the 61 values of o to 3 values of m. An exact reconstruction of o cannot be possible with the measured values. It can only be estimated from m, which leads to the research field of spectral estimation.

2.4   Spectral Estimation Methods

2.4.1   Introduction to Inverse Linear Problems

The above example of a 3 color camera shows the information loss in the measurement process. Depending on the measurement system, this loss has a different magnitude. Hyperspectral imaging systems lose in general less information than multispectral imaging systems. Spectral estimation methods compensate this loss of information. They are used to find a suitable solution for the linear inverse problem of solving equation 2.17 for the measured property o. This is usually an ill-posed problem [31]. A problem is ill-posed if it does not fulfill all conditions for a well-posed problem. These conditions are the existence of a solution, the solution being unique, and the continuous dependency of the solution on the problem data. The last condition is necessary for a stable numerical solution. It means that small variations of the problem data must not result in large variations of the solutions [31]. For linear inverse problems a large variety of methods to find a solution are available [31]. Which one of them is the best for a particular problem is often unclear. This is the reason why this work presents some methods for solving inverse linear problems that are used in the context of spectral imaging. The presented methods are then later evaluated experimentally with data from the built multispectral imaging system.

2.4.2   Preprocessing of Raw LED Multispectral Images

The raw data collected by the camera in a multispectral imaging system can usually not directly be interpreted as spectral samples. The illumination of the scene is probably not perfectly evenly distributed, the camera lens adds artifacts like vignetting to the image, and the camera sensor puts a noise offset to the data caused by dark current. Because of this, a correction of the acquired raw data is necessary. For this in general, two images are taken with the same system settings as the multispectral data. One image is for the correction of the dark current. It is taken with all lights off and is then subtracted from every other image. The second image is taken of a reference target with a spatially uniform and known reflectance. In the case of LED multispectral imaging, this has to be taken for every single LED-channel, as it is used to correct the uneven illumination in addition to the vignetting. This process is called Flat Field Correction and can be described by the following formula [29]:

$$R_s(\lambda) = \frac{I_s(\lambda) - I_d}{I_r(\lambda) - I_d} R_r(\lambda) \tag{2.18}$$

$R_s(\lambda)$ is the flat field corrected, relative reflectance image of the scene. I_s stands for the raw image of the scene, R_r is the reference target's reflectance and I_d is the dark image. In the context of LED multispectral imaging, the dependency of λ can be seen as LED peak wavelength. The Flat Field Correction makes every measurement relative to the reference target measurement.

This is why the typically multispectral imaging systems are limited to flat scenes where the light distribution on the reference target is known. Specially manufactured diffuse reflecting targets can be used for Flat Field Correction, but also other targets of Teflon or PVC have been used [50].

2.4.3 Spline Interpolation

The data from a hyper or multispectral imaging system can be considered as samples of the scene points spectral reflectance curves [31]. These samples can then be interpolated with smooth curves, for example, by cubic Spline Interpolation. The Spline Interpolation calculates the points between samples with polynomials of low order. The cubic C^2-spline is constructed out of polynomials of third order and has to be twice continuously differentiable. In the transition of the spline parts which are in the sample points, the first and second derivative of the corresponding polynomials are constrained to be equal [40]. An example of cubic Spline Interpolation is given in figure 2.10. It shows the spectrum of patch 2 from a color target introduced in section 3.5. For the example, the measurement interval was reduced to 20 nm. In this way, the shapes of the polynomials that connect two sampling points are better visible.
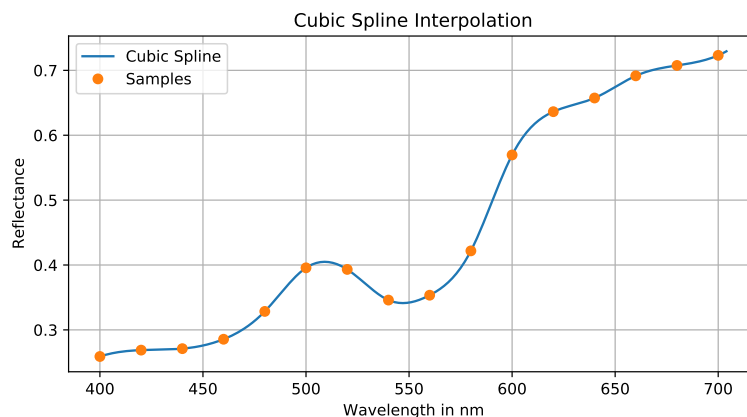
Figure 2.10: Example cubic Spline Interpolation of a color target with a sampling interval of 20 nm.

A challenge by assuming discrete samples is the positioning of the camera response samples in the spectral range. Neither a filter-based nor a LED-based system can provide an ideal sampling like classical Dirac delta functions. For narrow-band, Gaussian-like LEDs or filters the placement in the spectral range can be done with low uncertainty in the center of the band. For wider or not symmetrical bands the uncertainty rises [31]. No statistics are used for this method. Thus it profits significantly from a dense sampling, meaning the use of many LEDs or filters in the system. On the other hand, this method is prone to measurement noise and unable to compensate for outliers as the curve is fitted through every sampling point.

2.4.4   Wiener Estimation

Wiener Estimation and variations of this method are often used for spectral estimation from multispectral data. In that context, it is well described in [31] which is used as the information source for the following description of the method. Ignoring the measurement noise o from equation 2.17 could be directly reconstructed with the inverse of Φ: $o = \Phi^{-1}m$. But if Φ is not a square matrix, the inverse does not exist. The system is under- or over-determined and thus either infinite or no solutions exist. The problem is then ill-posed by the above definition. Here the under-determined case is presented, because it is more relevant for this work. The inverse can be replaced by the pseudo inverse which is for under-determined systems defined by

$$\Phi^- = \Phi^T (\Phi\Phi^T)^{-1}. \tag{2.19}$$

This offers a solution to the problem, but this solution is not necessarily stable. Wiener Estimation uses statistics to stabilize the solution. More specifically it uses the covariance matrices of reflectance spectra Ψ_o and of the measurements Ψ_m. The latter is modeling the system noise. The inversion by Wiener Estimation is then defined by the following equation:

$$\Phi^-_{wiener} = \Psi_o^{-1}\Phi^T (\Phi\Psi_o^{-1}\Phi^T + \Psi_m^{-1})^{-1} \tag{2.20}$$

When no detailed knowledge about the measurement noise is given, a white noise model can be chosen with the covariance matrix of $\Psi_m = \sigma_n^2 I$, where σ_n^2 is the noise variance and I denotes the identity matrix. In the case of a reflectance measurement, Ψ_o has to be calculated on a set of known reflectance spectra.

For this estimation method the measurement system matrix Φ must be known. For LED multi-spectral imaging it is constructed with the sensor sensitivity and the LED spectra. In this work, no measurement of either is done, because the necessary tools for that are not available. However, manufacturers give information about this in their datasheets. This will later be used to build the model for this work. If Φ is known accurately Wiener Estimation has theoretically the advantage that it needs no training data, which makes a target scene with known spectra redundant. In practice, such a target is still needed for the validation of the estimation method, which makes this advantage only theoretical. The same statement is also valid for the Spline Interpolation.

2.4.5   Regression Methods

A solution that does not need knowledge about the system is regression. Regression is estimating a model for the relationship between a dependent variable and one or more independent variables [46]. In this case, the dependent variable is the object property o and the independent variable is measurement vector m. A regression model is calculated based on pairs from the dependent and independent variables. This training data has to be generated before applying regression

methods. Consequently, for this type of methods, a target of known reflectances is necessary to be measured with the developed multispectral imaging system to build a set of training pairs. With this set it is possible to fit many regression models. A plausible one is a linear model, because equation 2.17 is also linear. By solving a least-squares problem the coefficients of the operator Φ^-_{linreg} are found. Thus, the desired property o is given by the following linear equation system:

$$o = \Phi^-_{linreg} m \tag{2.21}$$

Implementations of this are freely available and this work will use the Scikit-learn library [27]. Another far more complex regression model is the Gaussian Process Regression. It has been used to estimate spectra from RGB images in [1] and for multispectral data in [15]. The definition of a Gaussian Process is the following: "A Gaussian process is a collection of random variables, any finite number of which have a joint Gaussian distribution." [6]. It is specified by a mean function and a covariance function. A detailed description of it can be found in the source of the above definition. The purpose of the Gaussian Process Regression in this work is to investigate if more complex regression methods that can model non-linearities perform better on the problem. For this also a Scicit-learn implementation is used. However, because this is a complex method it would need more effort of optimization than the other methods. This cannot be provided in this work, so only one configuration with an radial basis function (RBF) plus a white noise kernel as covariance function, see [27], will be used in this work.

Chapter 3

LED Multispectral Imaging System Development

With the theoretical foundation set, this chapter covers the development of the multispectral imaging system until the point where it can be integrated into a 3D underwater imaging system. First of all, the conceptual design of a multi-band LED light source is described. This concept is then further developed and selected parts of the electrical, mechanical, and software design are presented. An important part of the development is the system calibration with a camera sensor. A model for this is here derived and validated. The calibrated raw multispectral data this system produces is then ready for spectral estimation. The above introduced methods are tested experimentally on a color target on which basis a decision for a spectral estimation method is made.

3.1 Conceptual Design

3.1.1 LED-Selection

The core part of an LED multispectral imaging system is its illuminant. Contrary to most other LED multispectral imaging systems, the system resulting from this work shall operate under difficult environmental conditions. The camera shall usually be mounted at an underwater vehicle, which is not only moving in the water, but also a source of vibrations and the scene might be dynamic due to the effects of the water current. This is reducing the maximum illumination time for motion distortion free pictures which increases the necessary amount of light. Another environmental factor that requires more light than laboratory setups are the effects of water and dissolved particles in it which are described in section 2.1.5. The attenuation in water is also limiting the wavelengths to the visible range. The system is also constrained to be as small as possible to make the later development of a pressure housing and integration into the underwater vehicles peripherals as simple as possible. This leads to the conclusion, that only high-power LEDs, that allow a high forward current, are suitable for the system development. This makes the selection of the LED-bands less complex because the variety of commercially available LEDs is much smaller. Consequently, the LED selection was more based on availability than looking for an optimal approach for a wider choice of LEDs as it was done by Shretsha et al. [35].
The approximated normalized spectra of the selected LEDs can be seen in figure 3.1.
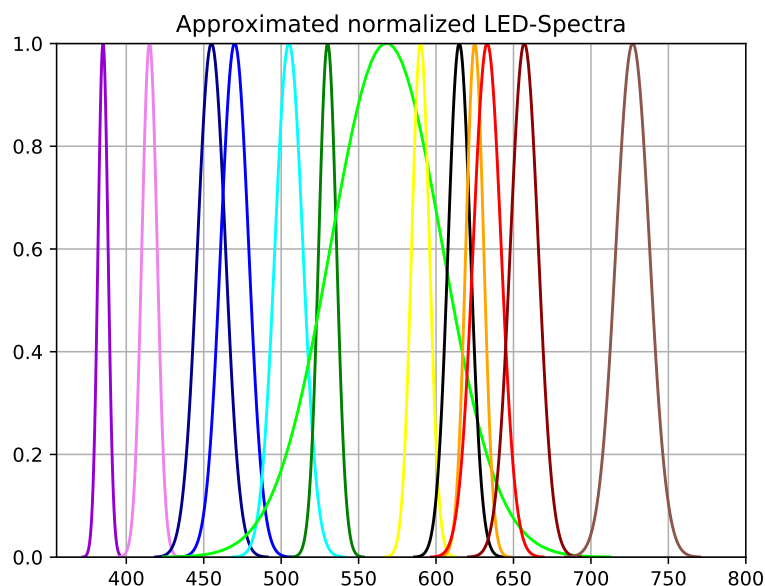
Figure 3.1: Normalized approximated spectra of the selected LEDs.
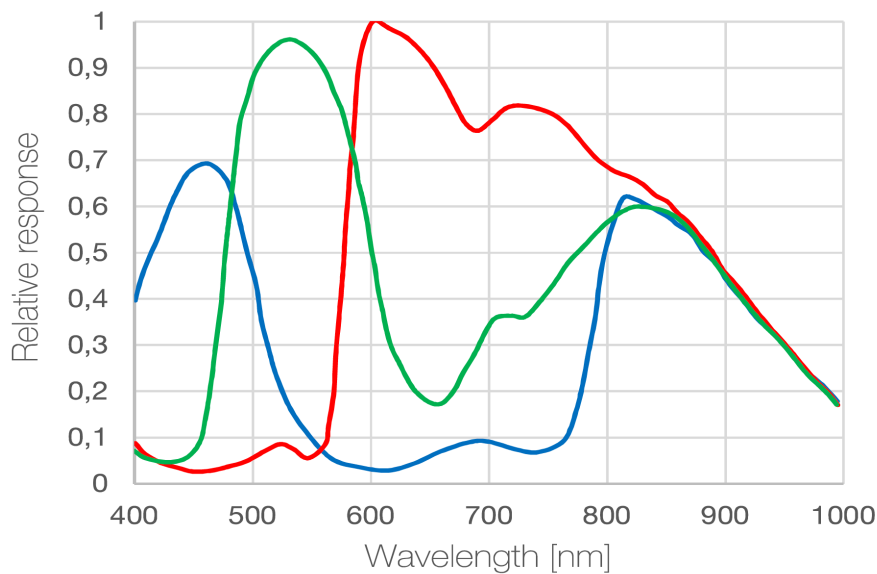
Figure 3.2: Sensor response of the used sensor module. Source: [11]

The approximation was done with datasheet values and the Gaussian function. Each was param-
eterized to have the peak at the corresponding LED's peak wavelength and match the LED's
typical spectral half-width. With this, the corresponding Gaussian function was parameterized to
match the spectral half-width at 50 percent of its peak magnitude. This simple model is relatively
accurate for narrow-band LEDs, but its error rises with the spectral bandwidth of the LEDs. But
since only the lime-colored LED with a peak wavelength of 568 nm has a significantly wider
band than the other LEDs, this model is used as an approximation.

The illuminant is later integrated into a 3D scanning system, which already contains a full HD
camera sensor. The 3D-scanner system is further described in section 4.1. The included camera
sensor will also be used to scan the scene in the spectral dimension. It is a Sony IMX290LQR
color CMOS image sensor whose relative response can be seen in figure 3.2

Another important property of the sensor is its linearity, because the spectral estimation methods
Wiener Estimation, Linear Regression, and Spline Interpolation require a linear measurement
of the light intensity. To verify the linearity of the camera sensor, a measurement series with
increasing exposures was taken. The result is shown in figure 3.3. It can be seen, that the response
of the camera is linear until saturation effects appear above a value of 250.

The next design question to answer concerns the quantity of each LED type. The goal is to
use a minimal amount of LEDs and create equal illumination conditions for each LED-channel.
By controlling the LED-channels individually, an equal illumination can be achieved for any
quantity of LEDs, but a solution is only optimal if all LEDs are driven close to their maximum
electrical ratings. The LEDs are different in their radiance and the attenuation of the water is
wavelength-dependent, consequently, the different LEDs are needed in varying quantities. Also
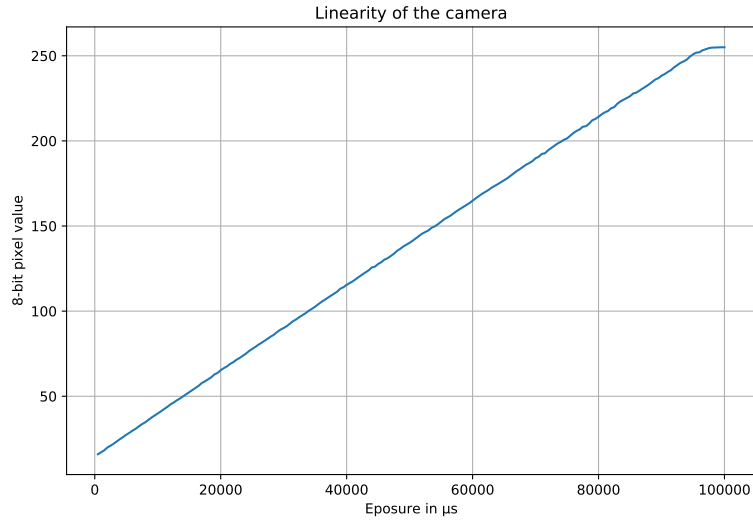
Figure 3.3: Experimental verification of the camera sensors linearity.

due to the water properties, the design can only be optimal in one distance for a specific water compound. The working distance is chosen to 1,5 m and the water type for the design is clear water, thus only the attenuation of water molecules is considered. For the calculation of the LED quantities, it was assumed that the light travels twice the working distance in clear water and that all light emitted hits the sensor. This way the calculation could be done by the LED's radiant flux independent from the LED's viewing angle since the viewing angle is considered in the LED selection and is similar for all LED-channels. Thus it can be neglected. With the Beer-Lambert law from equation 2.5 and the sensor response from figure 3.2 the quantities are calculated, assuming the LEDs are monochromatic with the peak wavelength. The attenuation coefficient for clear water, α_W, was taken from [28]. A plot which shows the wavelength dependency of the absorption coefficient has been presented in figure 2.5 of section 2.1.5. An overview of the LEDs is presented in table 3.1, where λ_{Peak} denotes the LEDs peak wavelength, P_{LED} is the corresponding data sheet value for the radiant flux, s_{max} is the maximal sensor sensitivity for the peak wavelength, P_0 is the overall emitted radiant flux, and P_{sensed} is the radiant flux that would be sensed according to above assumption. It is noticeable, that P_{sensed} is not even close to the real flux, that hits the sensor and is only used to calculate the LED quantities. The necessary P_{sensed} is calculated from the red light channel of the RGB LED, which is already installed in the 3D scanner system. The last row in table 3.1 shows a near-infrared LED. Although it was calculated that most of its energy will be attenuated by water, it is still included to later run some experiments with this wavelength. The ultraviolet LED with 385 nm can also be used outside the context of multispectral imaging, as corals can be excited with that wavelength [34], which creates another use case for the system in environmental monitoring.

λ_{Peak} (nm)	P_{LED} (mW)	Quantity	s_{max}	α_W (1/m)	P_{sensed} (mW)	P_0 (mW)
385	425	11	0.3	0.00941	1363	4675
415	725	4	0.45	0.00444	1288	2900
455	690	3	0.7	0.00962	1408	2070
470	591	3	0.7	0.0106	1202	1773
505	295	6	0.9	0.0256	1475	1770
530	195	9	0.95	0.0434	1464	1755
568	360	6	0.85	0.0672	1501	2160
590	240	10	0.9	0.1351	1440	2400
615	304	10	1	0.2678	1361	3038
625	422	7	1	0.2678	1323	2954
633	372	10	0.95	0.2995	1439	3720
660	400	14	0.85	0.41	1391	5600
730	280	17	0.8	1.678	25	4760

Table 3.1: LED-channel power information.

3.1.2 Spatial LED positioning

The LEDs are mounted on a printed circuit board (PCB). For the later integration into a cylindrical pressure housing, a circular design of the PCB is beneficial. For the electrical routing, it would be optimal, if the LEDs of one channel were placed close to each other, as each channel needs to have its LEDs connected in series. Contrary to that, thermal and optical considerations demand a uniform distribution of the LEDs. For the thermal considerations, it was assumed, that local heat would rather lead to damage than heat distributed over the PCB. Otherwise, a dense placement would be better thermally because of fewer conduction losses in the traces. From the optical viewpoint, it is plausible that a dense placement of LEDs could lead to uneven illumination of the scene. The last argument is the most important, hence the LEDs of each channel are placed to have a large distance between each other. The calculation of the LED positions was automated, as a manual placement would be time consuming and probably less optimal. The LED positioning algorithm starts with a random initialization in which one LED of each type is placed. To place a new LED, the distances to all already positioned LEDs of that channel are calculated for every free position. With a cost function, that penalizes short distances, the optimal position for the new LED is found. This method does not deliver an optimal placement for all LEDs, since the optimal position according to the cost function is only searched in the free positions, which might lead to a situation where only sub-optimal positions for a LED are left. But the cost function can be used to calculate a score that indicates the quality of the solution. A good solution can then be obtained by running the positioning algorithm a few times with different initial positions and
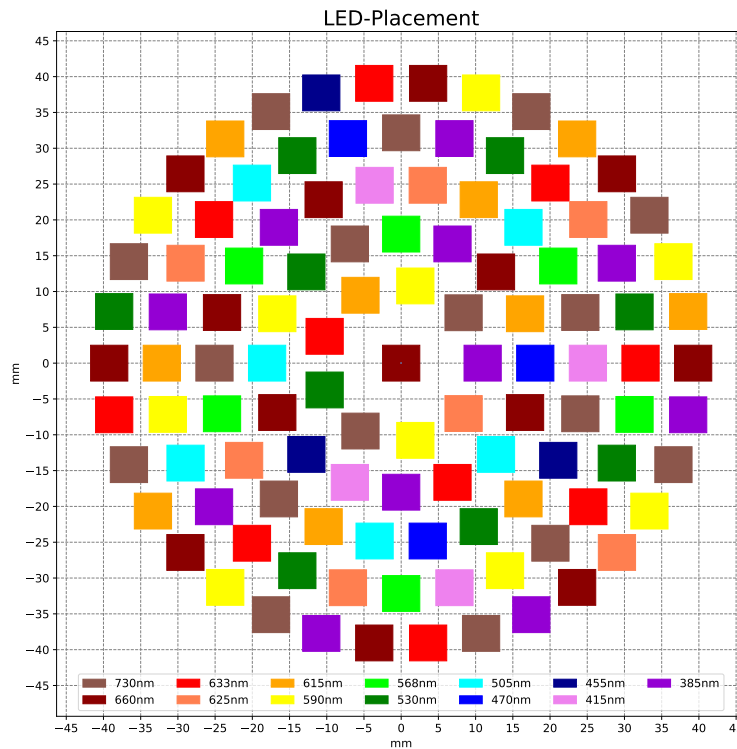
Figure 3.4: Solution of the LED positioning algorithm

then selecting by the score. The result from this procedure is shown in figure 3.4.

3.2 Electrical System Design

3.2.1 LED Board

Most selected electrical parts and all used LEDs are surface mount devices (SMD), which requires the design of a PCB. The electrical design consists of two PCBs: The LED board and the driver board, which are stacked together. This is easier to assemble than one two-sided PCB and it is practical for the further development. For example, may the same driver board be able to power different versions of the LED-Board. For the PCB design, the open source software KiCad [20] is used.

The LED board is designed as a round 2 layer PCB with 100 mm diameter. The copper layer thickness is chosen to relatively thick 105 μm to create good thermal conduction properties and reduce the risk of damaging the LEDs. Placing a large number of footprints in the PCB design is

a very time-consuming process. But because the LED positions are already digitally available, it is possible to automate this as well by using the python interface of KiCad. As all LEDs driven by one driver circuit have to be in series, the order of the LEDs matters. The connection of the footprint instances is defined by the schematic. Just placing arbitrary instances of a specific LED to any position for that LED-channel would lead to chaos in routing the copper traces, which is already harder because of the optical priority for the positioning. Consequently, the goal for the placing is to minimize the distance for the copper traces. This is done by calculating the distances between each LED and the in and outgoing connector. A first solution is then created by always going the shortest distance. This path is likely to be the shortest, but not guaranteed to be. To make this path then the shortest possible each LED of one channel is swapped with the others. After each swap, the path length is checked. If it is shorter, the path is the new solution and the swapping process restarts. Otherwise, the next swap is performed. If no single swap results in a shorter path, the solution is considered sufficient, although solutions that result only in a shorter path by swapping more than one position at once are not found.

The routing and placement of thermal vias for conducting heat to the back layer are done manually. The resulting LED board design can be seen in figure 3.5.
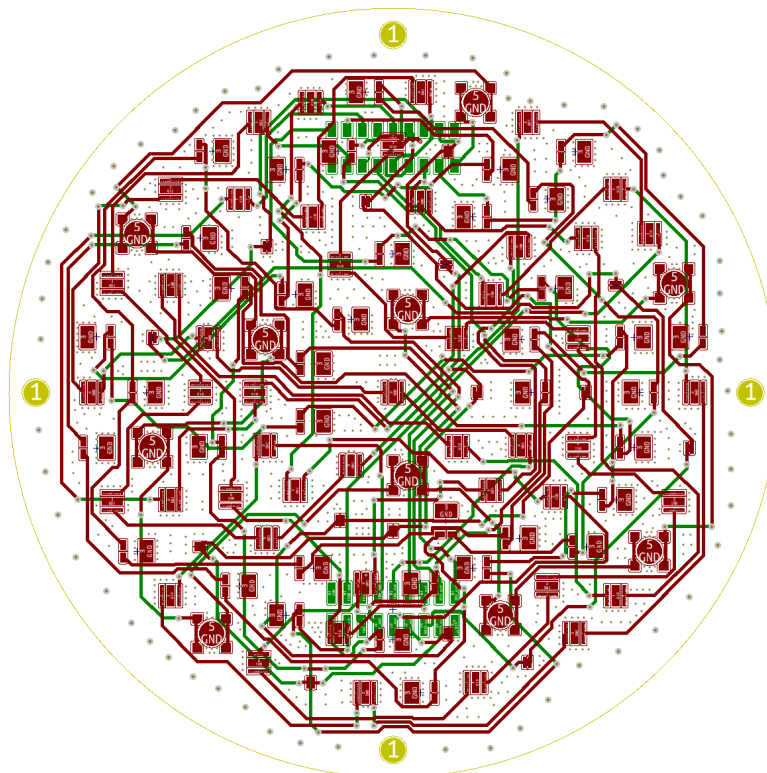
Figure 3.5: LED-Board routing. Red is copper on the front layer and green is copper on the back layer. Grey dots are vias and yellow circles are mounting holes.

3.2.2 Driver Board

The purpose of the driver board is to supply the LED-channels with current. The LEDs are driven by a constant current, which is modulated with pulse width modulation (PWM). The control of the LEDs needs to be as flexible as possible because future operations might require driving multiple LED-channels at once. This could be the case because of time savings in the multispectral imaging image acquisition or by using the LED board as a spectrally adjustable lamp for conventional underwater imaging. This results in the requirement to make the control of the LED-channels independent from each other. To drive each LED-channel individually the LED driver LT3476 from Analog Devices was chosen for the implementation. The integrated circuit (IC) has a small footprint and allows the control of 4 LED-channels at once. It can be seen as the core part of the driver board and is thus the only part to be described in more detail. Four drivers are needed for 13 LED-channels. In series, the forward voltage of the LEDs adds up. It exceeds the maximum rating of the driver in the case of the 385 nm, 660 nm and 730 nm LED-channels. These are divided into two channels resulting in the usage of all 16 available driver channels. The driver is implemented with a buck circuit configuration as depicted in figure 3.6. In the buck circuit, the driver works as a switching regulator, which converts up to 36 V to a lower voltage. The driver regulates the voltage over a 100 mΩ resistor which is in series with the LEDs. The setpoint for this voltage is programmed via an analog voltage at the VADJ pin of the IC. Digital control over PWM is also used. The capacitor and the inductor of the buck circuit are used as energy storage to supply the LEDs when the switch in the driver is turned off. The maximum duty cycle of the driver circuit and thus the ratio of input/output voltage is correlated to the switching frequency of the driver. Lower switching frequencies result in a higher duty cycle. But a lower frequency also means that the energy has to be larger. Therefore, the 4 drivers are implemented with different switching frequencies, to use the available space on the driver PCB more efficiently. The frequency is simply programmed over a resistor value. As the values of the inductor and capacitor change the properties of the control cycle, the circuits are simulated in LT-Spice to check for stability. The configuration in figure 3.6 shows the driver circuit for the red LED-channels, which need a high voltage because of their quantity. Therefore, the included inductor is relatively large with an inductance of $100\,\mu$H.

The other parts on the driver board PCB are mainly placed to operate the driver ICs. The most important of these is the microcontroller which is mainly used to generate control signals for the drivers and communication to a PC. The PWM signal is directly generated by the microcontroller while the analog control voltage for the driver setpoint is generated by additional digital-analog converters (DAC). These DACs are then controlled by the microcontroller via an I^{2}C bus. For communication, an Ethernet to serial bridge is included. Additional hardware to process a sync signal, that can be used to synchronize the light with the camera for later high-speed operation is also implemented. Electrically, the driver Board is designed to operate all LEDs at once with
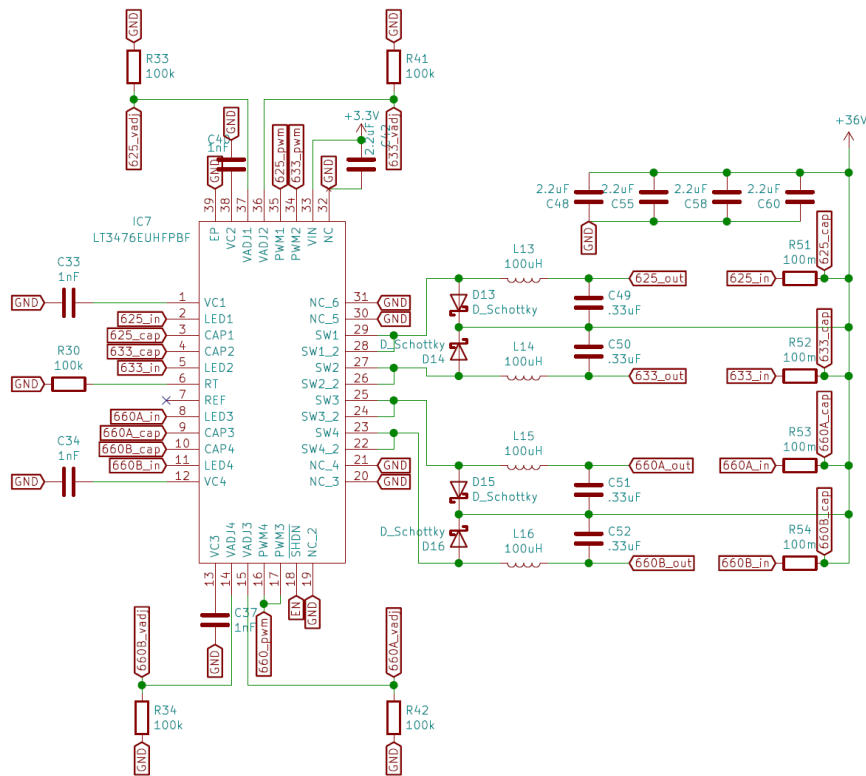
Figure 3.6: Configuration of the LED driver IC for the red LED-channels. The labels with a wavelength and the suffix *in* or *out* mark the anode of the first LED or the cathode of the last LED of the corresponding channel.

a maximum power of 1 A. This is equivalent to ca. 320 W of electrical power. But this is not the normal use case, as usually, only one or a few channels will be active at the same time. The thermal behavior at high currents and multi channel operation needs to be experimentally tested.

3.2.3 Embedded Software

The main function of the embedded software, that runs on the microcontroller, is to generate the electrical control signals for the driver and supply a communication interface to make the system controllable over network. The software builds upon existing firmware from KRG, where the communication part is already solved, leaving only the task to control the driver for this work. The software uses FreeRTOS, a real-time operating system for microcontrollers and the software part for controlling the LED drivers, is written in c++. The original firmware was extended by two classes. The first one is implemented to abstract the usage of the DACs. It does the addressing on the I^2C bus and provides methods to change the analog output voltage of the different DAC channels. The second class is representing one LED-channel. It has an instance of the first

class, assigning the corresponding DAC and its specific channel to it. The DAC output voltage is controlled by setting the desired current for the LED-channel. The second control parameter for the LED-channel class is the digital modulation of the LEDs, which is done by a PWM signal. This is directly generated by the microcontroller and it can be activated and adjusted over the LED-channel class. The desired LED current and the PWM duty cycle are adjustable over network, as well as a 13-bit value indicating which LED-channel is active. The synchronization with the camera is not yet implemented, since this work is focused on presenting a multispectral imaging system prototype. Software for the high-speed use case can be implemented later.

3.3 Development of a Pressure Housing

For the operation underwater, it is necessary to provide a waterproof housing for the electronics that can resist outer pressure. This requirement is based on the use case. For the laboratory experiments, waterproof would be enough, since depths of more than one meter are not possible. For field operation the situation is different. The multispectral imaging system has use cases in all depths. Consequently, the housing is designed to resist high pressure. The concept for the housing can be seen in the explosion view in figure 3.7. The electronic is mounted in a cylindrical container. It is equipped with an outer thread and an O-ring groove on top. An O-ring is placed in it and compressed by a glass window which is pressed on by a large nut that is screwed on the container thread. At the bottom, a connector for underwater applications is mounted. The connector is a DBH13M from SubConn Inc. with 13 contacts and an Ethernet cable. It is sealed by another O-ring that is pressed against the container by a nut from the inside. A section view of the assembly is provided in figure 3.8. There it can be seen that the wall thickness of the container is not constant, as there is more material at the bottom. This has two reasons. One is the increased
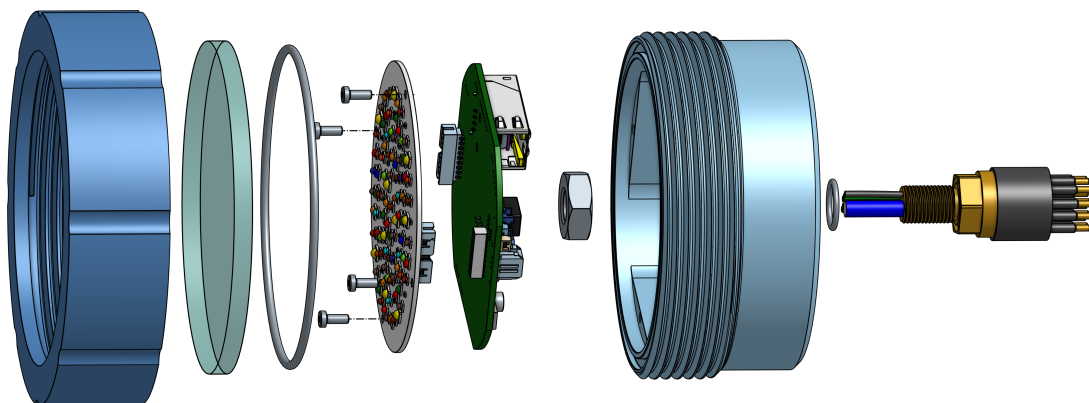
Figure 3.7: Explosion view of the pressure housing assembly.

resistance to outer pressure and the other one is flesh for drill holes. These may be needed for mounting a sacrificial anode from the outside or for alignment in a mounting system. From the inside, this can be used for heat pipes to transfer heat from the electronics to the housing. If further heat solutions are required, has to be tested in the later operation of the system.

The calculations for the design of the O-ring groove were done with the ERIKS O-Ring calculator [10] and the selected O-Ring is made of Buna-N Rubber with a hardness of 70 A, a width of 3 mm and 105 mm inner diameter. For the pressure calculations, the software provided by Blue Robotics
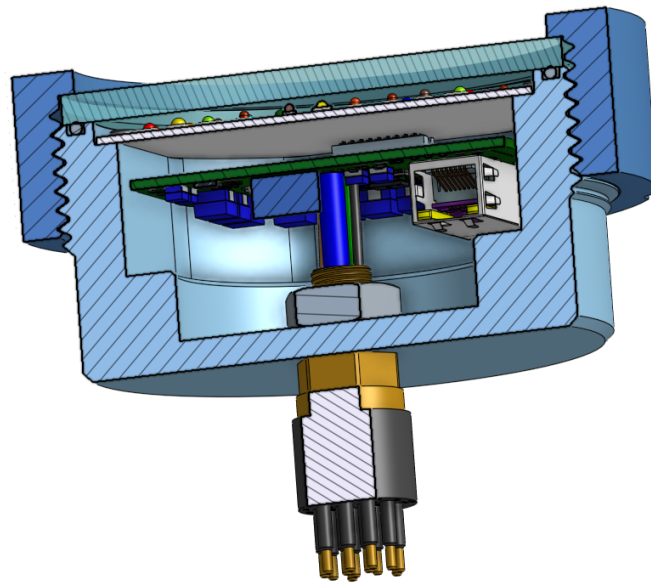
Figure 3.8: Sectional view of the pressure housing assembly.

Inc. [4] was used. This resulted in a calculated failure of the container at a depth of 1100 m in seawater if it is manufactured from aluminum. The large glass window however is pressure-wise the greater problem. The installed glass window of 6,35 mm thickness is calculated to break at a depth of 42 m. This is enough for some field experiments. But to match the possibilities of the aluminum container, the glass window has to be 32,5 mm thick. Because mainly the glass thickness determines the depth rating of the housing, it is designed to fit different window sizes. The glass can be replaced without any other changes at the housing.

For the laboratory experiments, it was tried to manufacture the housing with fused deposition modeling (FDM) 3D printing. The print was done with PETG and it was further processed with sanding and an epoxy surface finish. But a sufficient surface quality on the top O-ring groove was not achieved and the fully 3D printed housing was not waterproof. A waterproof housing was then achieved by letting the container be CNC manufactured out of aluminum and anodized afterwords. The large nut that was used to press on the glass window remained 3D printed.

3.4 System Calibration

3.4.1 Flat Field Model

As described in section 2.4.2 it is necessary to perform a Flat Field Correction on the images taken by the system. Contrary to other systems the distance to the target is not constant and that is why classical Flat Field Correction cannot be applied. But the knowledge about the distance of any scene point to the camera can be used to provide something similar. If it were known how much light hits a scene point, then its reflectance can be determined. Otherwise, the measured reflectance would be affected by the position of the scene point relative to the system, because the light is not evenly distributed over the scene. The information must be known for every light channel because the light distribution is slightly different for every channel. With this information Flat Field Correction can be performed for the point cloud as in a 2D image by dividing each measurement point by the value it should have as a perfect reflector. To provide the needed information a model assumption is made. It was assumed that the light distribution of the light source follows a 2D Gaussian distribution and the camera sensor behaves linearly. The system model for one dimension is depicted in figure 3.9. For simplification, all the following considerations are presented for the horizontal dimension. The vertical part is analog to it.
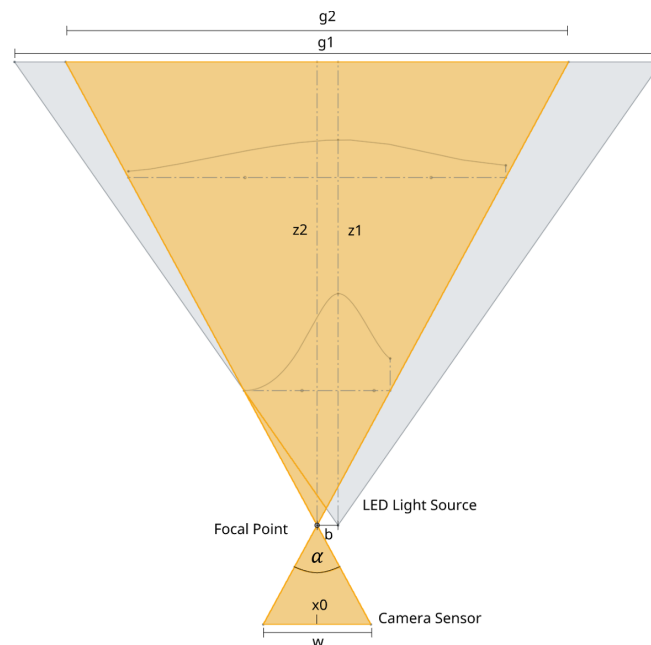
Figure 3.9: One-dimensional depiction of the system model. The light distribution of the Light source is modeled as a Gaussian distribution. The distributions seen by the camera are given for two distances in the image. The light seen by the camera is represented in yellow.

The camera and the light source are placed in the same plane. The figure shows both, the light cone from the source and the cone that is seen by the camera. The two Gaussians in the figure represent the light distribution at two distances seen by the camera. The dotted line can be interpreted as a pixel line on the sensor and the values of the Gaussian are then proportional to the pixel measurements. If z is the distance to the camera, the measured pixel value is modeled to decrease proportionally to a factor of $\frac{1}{z^2}$. This is justified by the fact, that the illuminated area is increasing proportionally to z^2. With an increasing z, the peak of the function moves further to the image center. This means for the model in pixel coordinates that the position of the peak is dependent on the ratio of the extent of the imaged scene and the distance between camera and light source, the baseline b. From the geometry in figure 3.9 the following relation for this can be derived:

$$\mu = x_0 \frac{\frac{1}{2}w \cdot b}{z \cdot \tan(\frac{\alpha}{2})} \tag{3.1}$$

Where μ indicates the mean in the Gaussian distribution function, x_0 is the image center position in pixels, α is the viewing angle of the camera and w is the sensor's width in pixels. b is allowed to be negative and the sign indicates if the peak is left or right of the image center. The parameters of the model are later fitted, thus it is for numerical reasons easier to describe equation 3.1 with all constants joined in one constant c:

$$\mu = x_0 + \frac{c}{z} \tag{3.2}$$

The last parameter of the Gaussian model is σ and the question is if the standard deviation changes with the distance z in the pixel coordinates. It is plausible that the 1σ points in the light cone lie on the surface of a cone within it. Consequently, σ rises with a higher distance seen from the outside. But the extent of the imaged scene is also rising with a growing distance. This is leading to no change of σ in pixel coordinates. This can be shown with the following consideration: If the ratio of g_1 and g_2 from figure 3.9 is independent of z_1 and z_2, the distance of the 1σ points in the image stay the same. The ratio is given in the following equation:

$$\frac{g_1}{g_2} = \frac{2\tan(\frac{\beta}{2})z_1}{2\tan(\frac{\alpha}{2})z_2} \tag{3.3}$$

Where β denotes the opening angle of the LED light cone. This makes it plausible, that σ does not change, as long as the light source and camera are mounted in the same plane and, therefore, fulfill the condition $z_1 = z_2$.

The above model assumptions lead to the following 3D model:

$$f(x,y,z) = A\frac{1}{z^2}exp\left(-\frac{(x-(x_0+\frac{c_x}{z}))^2}{2\sigma_x^2} - \frac{(y-(y_0+\frac{c_y}{z}))^2}{2\sigma_y^2}\right) \tag{3.4}$$

Where x and y are pixel positions and z is the distance to the scene point in mm. It returns a value that can be used to perform Flat Field Correction for a given scene point.

The above model assumes a perfect alignment of the camera and the light source. To account for some imperfections in the setup, a combination of $f(x,y,z)$ with different parameter values is used as a model:

$$l(x,y,z) = f_1(x,y,z) + f_2(x,y,z) \tag{3.5}$$

3.4.2 Flat Field Model Validation

The purpose of the model validation is to test if the model is accurate enough for the use case. The above model is a core part of the multispectral imaging system and thus needs to be validated before use. This was done with a test setup in a dark room with the built light source and a monochromatic version of the introduced camera sensor. For the parameterization of the model, a white wall was photographed with the system at 10 different distances. For the validation, only one LED-channel was used and the images were further processed by subtracting a dark image, blurring, cutting out the 1000x1000 pixel image center. For computing performance reasons every 10th pixel was used for the parametrization. Values in the range from 20 to 235 were then used to fit the model using the *curve_fit* function from the SciPy optimization library. Table 3.2 shows the performance of the single Gaussian model $f(x,y,z)$ versus the double Gaussian model $l(x,y,z)$ with error metrics. MAE is the mean absolute error and MAPE is the mean absolute percentage error. They are defined by the following equations [44],[45]:

$$MAPE = \frac{1}{n}\sum_{t=1}^{n}\left|\frac{A_t - F_t}{A_t}\right| \tag{3.6}$$

$$MAE = \frac{1}{n}\sum_{t=1}^{n}|A_t - F_t| \tag{3.7}$$

It shows how capable the models are to represent the system. Both models show a relatively low error, considering that the data is not perfect, because the wall shows some imperfections. But the double Gaussian model outperforms the single Gaussian model in both metrics. In these equations, A_t denotes the actual values and F_t is the predicted value. The choice for these metrics is made because their results can be easily interpreted. The average difference for the double Gaussian model prediction to the test images is less than 2 in absolute pixel values. The better performance of the double Gaussian model may be reasoned in the ability to model an asymmetric light distribution. The downside of the double Gaussian model is the large number of parameters that can lead to numerical problems in finding the optimal parameters. Nevertheless, the better accuracy led to the decision to use the double Gaussian model to perform the Flat Field Correction in the multispectral imaging system.

Metric\Model	$f(x,y,z)$	$l(x,y,z)$
MAE	2.279	1.578
MAPE	0.063	0.053

Table 3.2: Comparison with error metrics of the single Gaussian model $f(x,y,z)$ and the double Gaussian model $l(x,y,z)$.
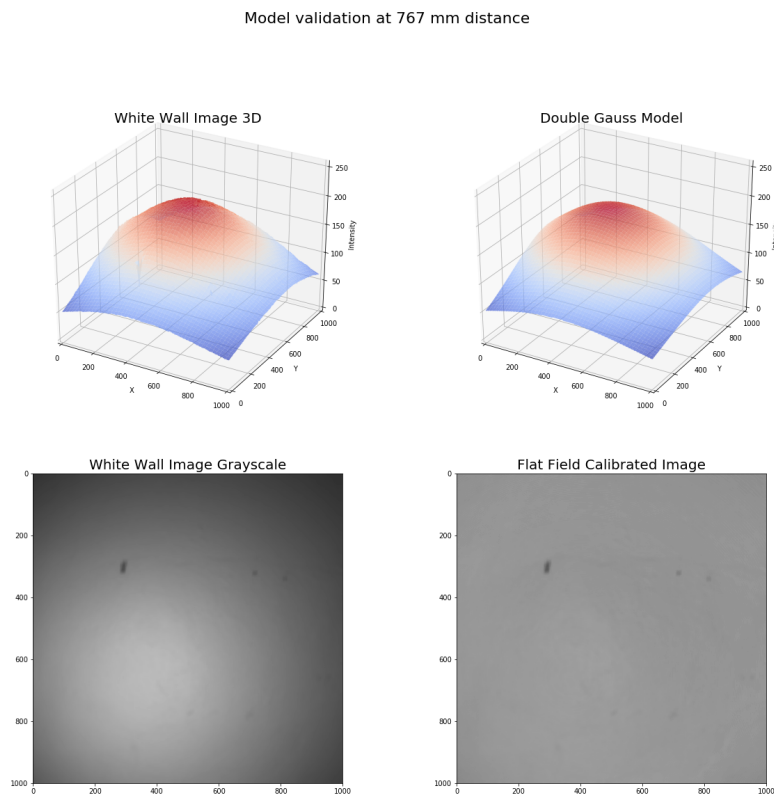
Figure 3.10: Exemplary image of the Flat Field Correction. It shows two representations of the white wall image (both left). One is 3D, which can be compared to the model output for that distance (top right). The other representation is a grayscale image, which can be compared to the Flat Field calibrated image (bottom right).

Exemplary, in figure 3.10 the performance of the model with $z = 767$ is visualized in a 3D plot. It shows an image of the white wall taken from 767 mm distance as a 3D plot, as a raw grayscale image and as the Flat Field calibrated image. The double Gaussian model output for that distance is also given in the figure as 3D plot. The 3D plots show high similarity. And although the images are blurred, some structures of the wall can still be seen. Especially the nail which was used to

place a target for computer vision distance measurement. The calibrated image was scaled to a value of 150. It shows, like intended, no dark corners and no bright spot in the middle of the picture, as the original image does. It is an even gray, without visible failures of the Flat Field Correction. The results for other distances look similar.

The flat fielded image is be the basis for spectral estimation methods and should thus be as good as possible. The double Gaussian model shows results above expectations, which would be even better with a better calibration target. It can thus be validated for further application.

3.5 Dry Evaluation of Spectral Estimation Methods

3.5.1 Experiment Introduction

To this point, the system with the Flat Field Correction is capable of taking multispectral images. But for this grayscale images of each illumination are necessary to allow an interpretation of the single images as samples at the corresponding LED's peak wavelength. A grayscale sensor can be used for this or the color images can be transformed into grayscale images. The latter option is less favorable, because the demosaicing in the transformation process from the sensors Bayer mosaic to the grayscale image introduces some errors during the calculation of the final pixel values. The obtained multispectral image is then a stack of 13 pictures, one for each LED-channel. It was decided to equip the multispectral imaging system with a suitable spectral estimation method to convert the collected flat fielded data into a spectrum for each pixel with 5 nm resolution. This allows the use of RGB sensor data. From the definitions of hyper- and multispectral images, this step estimates a hyperspectral image from the multispectral data. To distinguish the data types the result of this estimation step will be called a hyperspectral image, although the measurement data is only multispectral. Because of this, the system will be continued to be described as a multispectral imaging system despite having a hyperspectral image as output. The candidates for spectral estimation are Spline Interpolation, Wiener Estimation, Linear Regression, and Gaussian Process Regression. These methods were introduced in section 2.4. The suitable spectral estimation method is found experimentally on a dry setup.

3.5.2 Experiment Setup

For the evaluation, ground truth data is needed. For this, a *X-Rite ColorChecker Classic-Target* with 24 color patches was used. The target is depicted in figure 3.11 and its patches will be referred to as numbers starting with one for the top left corner and increasing left to right. It is widely used in the field of color science. Despite this, there are no spectral measurements published for the version after November 2014, which uses a new color mixture [49]. First trials

with obsolete data showed a significant difference. Consequently, new spectral data had to be recorded. This was done with a *BYK-mac i 23 mm* multi-angle spectrophotometer. The decision on which angular data will be used is not easy, because the light ray angles in the image change continuously and some effects caused by that are already indirectly compensated with the Flat Field Correction. For the device, the viewing angles are measured from the point of specular reflectance which thus refers to an angle of 0 degrees. Because the target is not placed far away from that point, 15-degree data is used. The obtained data lies in the range between 400 and 700 nm and is thus limiting the system, which has LED peaks from 380 to 727 nm. For still being able to reconstruct 5nm hyperspectral images as intended the ground truth data was interpolated with Spline Interpolation. The error resulting from this step is expected to be small because of the smooth characteristics of the target's spectra.

For the experiment, the LED light source was mounted next to the camera which uses the color sensor. This setup is shown in figure 3.12. The setup was pointed to a white wall which was imaged for Flat Field Correction. The calibration was performed on images of 15 different distances between 770 and 2200 mm. The distance in each picture was calculated with an AprilTag and software from KRG. For the Flat Field Correction, the Bayer pattern of the raw images was transformed into a grayscale image using OpenCV. During the correction process, it occurred, that the wall is not reflecting the light of the 380 nm LED. This is a good example of the information in multispectral data, but in this case, it caused the LED-channel to be left out for further processing. For the acquisition of the multispectral data, the ColorChecker target was placed at a distance of 1200 mm. The Spline Interpolation was performed on calculated grayscale images. The other estimation methods used the RGB filter responses of the camera sensor. The correction parameters from the gray images was then applied to the raw image because the light distribution only varies in the intensity of the different filter responses. This caused the Flat Field corrected

Figure 3.11: X-Rite ColorChecker Classic-Target. Source: [48]*(modified)*
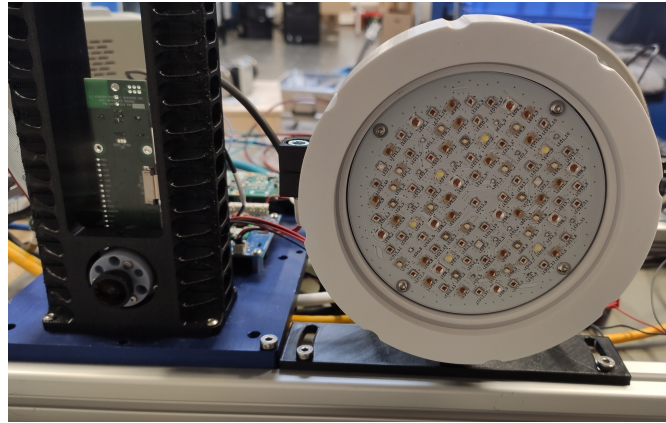
Figure 3.12: Setup for the dry experiment. The picture shows the alignment of the LED light source and the color camera.

filter responses to be in different ranges. After Flat Field Correction, the main contribution for the raw image contained sometimes values higher than 255. This did not cause problems, because the images could be normalized before applying the spectral estimation methods.

3.5.3 Implementation of Spectral Estimation Methods

The Wiener Estimation was programmed in python. The necessary covariance matrices of spectra were calculated from the Munsell data set provided by the Computational Spectral Imaging group from the University of Eastern Finnland [7]. This data set contains 1269 spectra of matte colors in the range of 380 to 800 nm with a resolution of 1 nm. The measurement system model was calculated from the LEDs and Sensor data sheets and the gain of the system was guessed, as there were no tools to measure the system. For the light source part in the model, the same approximation as already shown in figure 3.1 was used. The ground truth data of the ColorChecker board was then used to calculate a correction factor for the Wiener Estimation input data: The ground truth spectrum of patch 20 was multiplied with the measurement matrix and results in the camera measurements that would be expected if the system model was perfectly accurate. These simulated measurements were then divided by the average measurements from the color patch by the real multispectral imaging system. The result was the correction factor. This way, the gain of the measurement model fitted the input data for the Wiener Estimation. The noise variance for the Wiener Estimation was determined experimentally to minimize the error on the test data. The optimal variance for that experiment was found with $\sigma_n^2 = 2.9$.

The other methods do not require information about the measurement system. Both, the Linear Regression and the Gaussian Process Regression, were used from their Scikit-Learn implementation [27] and the Spline Interpolation was used from the SciPy library [38]. The samples for the

Spline Interpolation were assumed to be at the peak wavelength for each LED channel. For a direct usage of the pixel values, the Flat Field Correction would have been necessary on a target with a uniform reflectance of 1 for all wavelengths, or the spectral reflectance must have been known to correct the brightness of the different LED channels. A uniform reflectance is not provided by the calibration wall and neither is the spectral reflectance of the white wall known. To compensate for this effect, the brightness correction of the samples for the Spline Interpolation is done with patch 20.

The training data of the Gaussian Process Regression consist of the average pixel value of each patch because this method is prone to overfitting. For the Linear Regression, no averaging is done and the method is trained with every pixel of the corresponding patch. This way noise is modeled indirectly, as proposed by [31]. To further lower the influence of noise for the regression methods, filter responses with a low signal were sorted out. The remaining LED-Filter combinations are shown in table 3.3.

LED	385	415	455	470	505	530	568	590	615	625	633	660	730
Filter	/	B	B	G/B	G/B	R/G	R/G	R/G	R/G	R/G	R/G	R/G	R

Table 3.3: LED Filter combinations used as regression inputs.

3.5.4   Results and Evaluation

All implementations of spectral estimation methods were evaluated with the ColorChecker target. The multispectral data was averaged for each patch before estimating the spectrum for evaluation. Because the target only consisted of 24 patches, the ground truth data for the regression methods was divided into a training set of 23 patches and a test set of one patch for each patch of the color checker target. Consequently, it could be seen how well the model behaved for data outside the training set. For example, the regression models had not been trained on white data when they were estimating the spectrum of the white patch (patch 19). For an illustration of the estimation performances, the reflectance reconstructions is shown for a few example color patches in the following evaluation. The reconstruction of all 24 patches can be found in the appendix.

Figure 3.13 shows the performance of the estimation methods for the two brightest achromatic patches. Patch 20 was used as brightness correction for the Spline Interpolation. Because of this, the samples were perfectly aligned with the ground truth. The nearly equally good performance of the Spline Interpolation on the brighter patch implies that the Spline Interpolation is a suitable method for estimating achromatic spectra from the system's multispectral data. The sample at 660 nm can be seen as an outlier because it was caused by saturation of the red color channel of the camera. The error caused by this was very significant and led to the conclusion that the Spline Interpolation would not deliver stable estimations on noisy data. Especially, when the
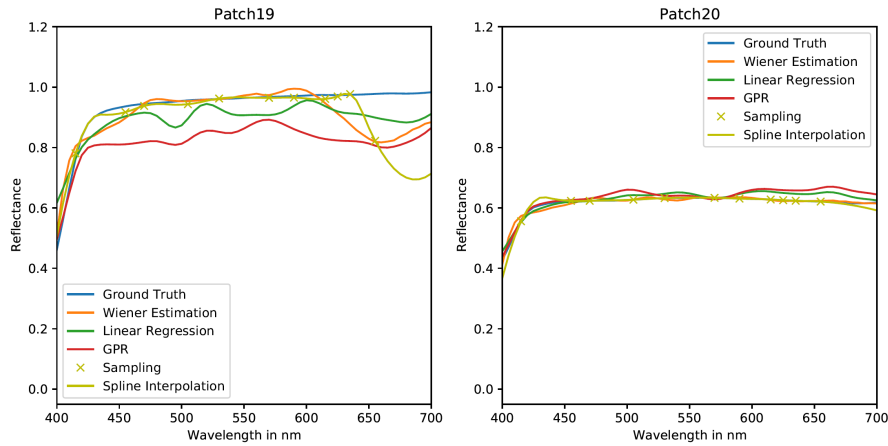
Figure 3.13: Comparison between the different estimators on the two brightest achromatic patches. The outlier in patch 19 is caused by saturation of one camera channel.

distance to the next sample is large, like in the example of patch 19 where the next sample was at 727 nm. The other estimation methods behaved a bit more robust to this outlier, but they also showed a large error on patch 19. Figure 3.14 shows exemplary the reflectance estimation
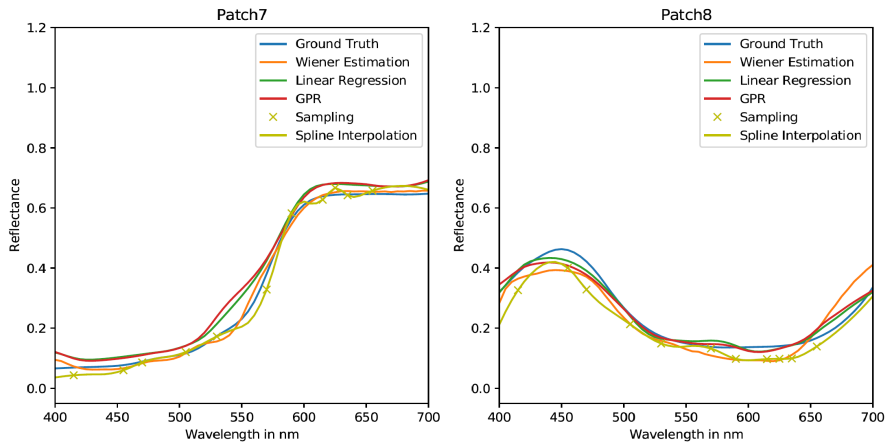
Figure 3.14: Comparison between the different estimators on two color patches.

for 2 achromatic color patches. Here, the Spline Interpolation was not able to sustain the good performance from the achromatic color patches. But the subjective impression from looking at the reconstructed spectra is that all methods resulted in a useful reconstruction of the spectrum. To make an objective evaluation of the methods error metrics are necessary. A common metric for this is the root mean square error (RMSE) which has a disproportionately large effect on larger errors. It is defined as follows [47]:

$$RMSE = \sqrt{\frac{1}{n}\sum_{t=1}^{n}(A_t - F_t)^2} \qquad (3.8)$$

In this particular case, A_t is the ground truth value for the reflectance at wavelength t. $t = 1$ corresponds to 400 nm and $t = n$ is for 700 nm. F_t is the corresponding forecast value. For some cases, a percentage error might be more useful. Thus, the mean absolute percentage error (MAPE) is also be used for the analysis. In this case, the MAPE allows a simpler interpretation as its meaning is the average percentage deviation of the estimated spectrum from the ground truth measurement.

Figure 3.15 shows the RMSEs from all estimation methods for every patch of the ColorChecker. It can be seen that for many patches the Spline Interpolation showed the largest RMSE. It can also often be seen that the performance of the Wiener Estimation was closer to the Spline Interpolation. The patches 7, 8, 10, 11, and 12 showed a high error with both of these methods. This correlation might be caused by the common use of patch 20 to adjust the gain. Looking back at the spectra in figure 3.13 it can be seen that the shapes of the spectra from patch 7 and 8 were predicted well, but in patch 7 the regression spectral estimations were above the ground truth spectrum and at patch 8 the Wiener Estimation and Spline Interpolation are mostly below the ground truth. This reinforces the assumption that the common gain adjustment is one reason for the error correlations. The errors of the regression methods also seem to correlate but the Linear Regression showed except for patches 21 and 22 always a lower error than the Gaussian Process Regression.
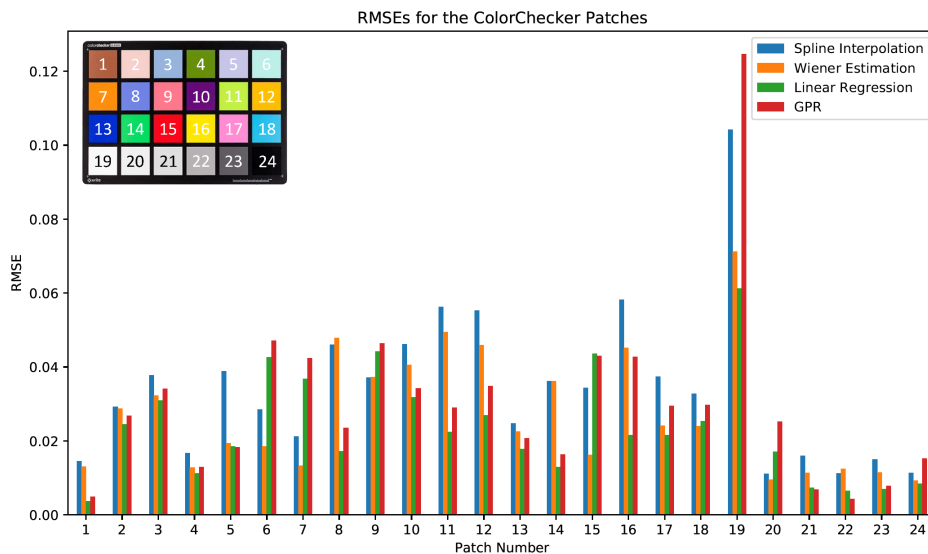
Figure 3.15: RMSE for the 24 ColorChecker patches and all estimation methods.

A look at the MAPE in figure 3.16 shows that the percentage error was high for dark patches. This can be seen in the increase of the MAPE for patches 22, 23, and 24. The large RMSE from patch 19 did not show in the MAPE of that patch because of the patch's high brightness. For patch 15 on the other hand the MAPE rose to nearly 40 percent with the regression methods, while there was no sign for this large error in the RMSE of that patch. This is caused by an error
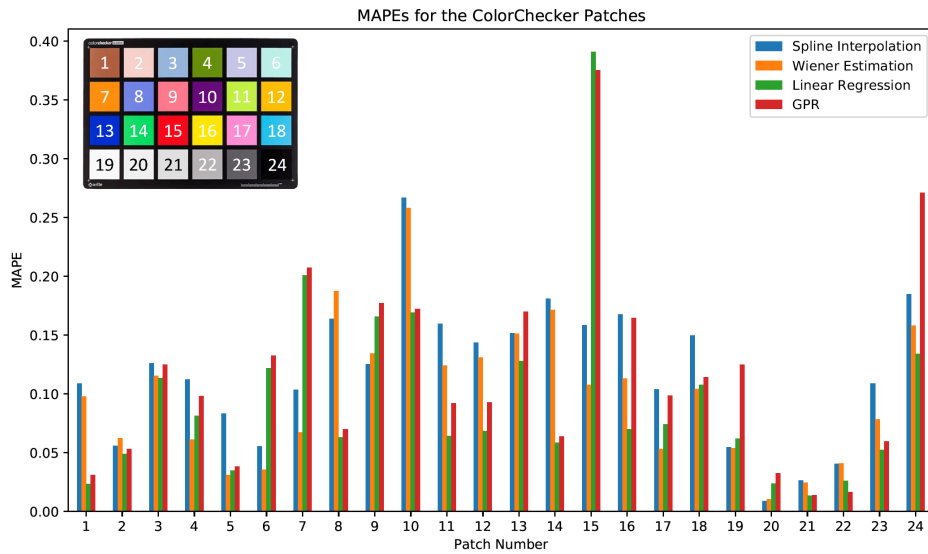
Figure 3.16: MAPE for the 24 ColorChecker patches and all estimation methods.

Method/Metric	RMSE	MAPE
Spline Interpolation	0.0341	0.118
Wiener Estimation	0.0272	0.098
Linear Regression	0.0234	0.096
GPR	0.0300	0.116

Table 3.4: Average error metric scores of the estimation methods.

in the estimation of the regression of the low reflectance part of that patch. However, not all dark patches showed a large MAPE. For example the spectrum of patch 1 was estimated very well with the Linear Regression. Despite the outlying performance on patch 15, the average MAPE of the Linear Regression method over the 24 color patches was still slightly below the average MAPE of the Wiener Estimation, see table 3.4. As Linear Regression had the lowest average RMSE and MAPE it was chosen as the spectral estimation method for the system.

Chapter 4

Application to 3D underwater Imaging

The above developed light source is ready for integration into a 3D underwater imaging system. This chapter describes the formation of the final underwater 3D LED multispectral imaging system and the data processing pipeline, which leads to a hyperspectral depth image as the outcome of the system. Finally, the system is tested in a water tank setup to show its capabilities.

4.1   3D System integration

4.1.1   Seavision System Introduction

To this point, the calibrated multispectral imaging system is capable of acquiring hyperspectral images of planes in different, but prior known distances. To make full use of the developed system, it needs to be integrated into a 3D underwater imaging system. The only requirement of the system is the ability to match pixels of a photo from the scene to its 3D measurements. The system of choice with this ability is the Seavision 3D scanner, provided by KRG. In this work, only a short overview of Seavision and its working principle is provided. A detailed work about this was done by A. Duda [8].
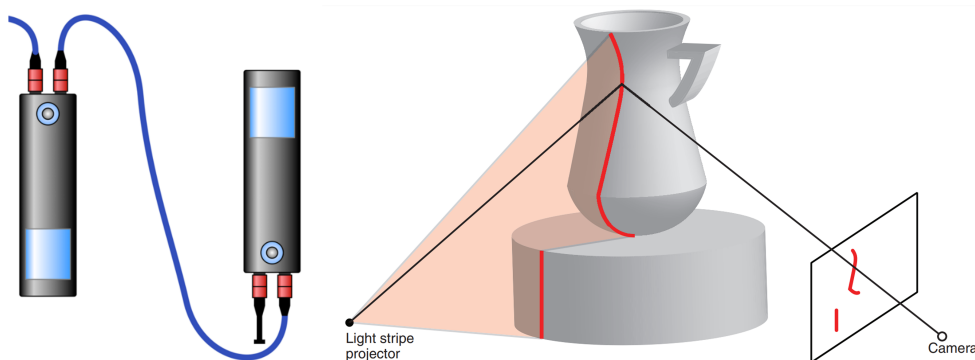
Figure 4.1: Left: Illustration of the Seavision System. Source: KRG. Right: Principle of structured light 3D imaging. Source: [30]

The Seavision System is illustrated left in figure 4.1. It is build of two units which each contain a line laser and a camera with the above mentioned color sensor. To obtain 3D information Seavision uses the laser one unit to scan over the field of view from the other unit. The term structured light refers to that method of 3D data acquisition. A depiction of its operation principle is provided right in figure 4.1. In this implementation of structured light, a line laser is swept over the scene and is observed by a nearby camera. The laser line will appear distorted from the camera's perspective. With an accurate calibration of the system, the camera response and laser angle measurements can be used to reconstruct the 3D scene with triangulation [30]. Because the camera sensor is used to obtain the 3D information, the needed reference from the 3D point to the corresponding pixel is automatically incorporated.

4.1.2   3D Multispectral Imaging Setup

The hardware integration was straightforward. The LED light source only needed to be mounted in the same plane as the Seavision's camera. Both, the Seavision System and the LED light source were then controllable over network. A series connection of the systems in general possible but might lead to problems when the LED light source is driven at high currents. In that case, some LED-channels would need above 24 volt, which would exceed Seavision's maximum voltage rating. This could be resolved by placing a DC/DC converter in the light source housing. However, for the prototype, an external power source was chosen. The synchronization between the systems for high-speed data acquisition was not yet implemented. Consequently the LEDs were driven carefully at a maximum current of 350 mA to not overheat them during long on-times.

Figure 4.2: Diagram view of the data processing steps.

Figure 4.2 shows the processes and intermediate products on the way from the scene to the final hyperspectral depth image. The processes are described as follows:

Laser Scanning: The scene gets 3D scanned by Seavision. The result is raw scan data.

Point Cloud Calculation: The raw scan data is processed to a 3D point cloud. For every point the corresponding sensor pixel position is known.

Depth Image Calculation: The point cloud is further calculated to a depth image. At this step, information gets lost, 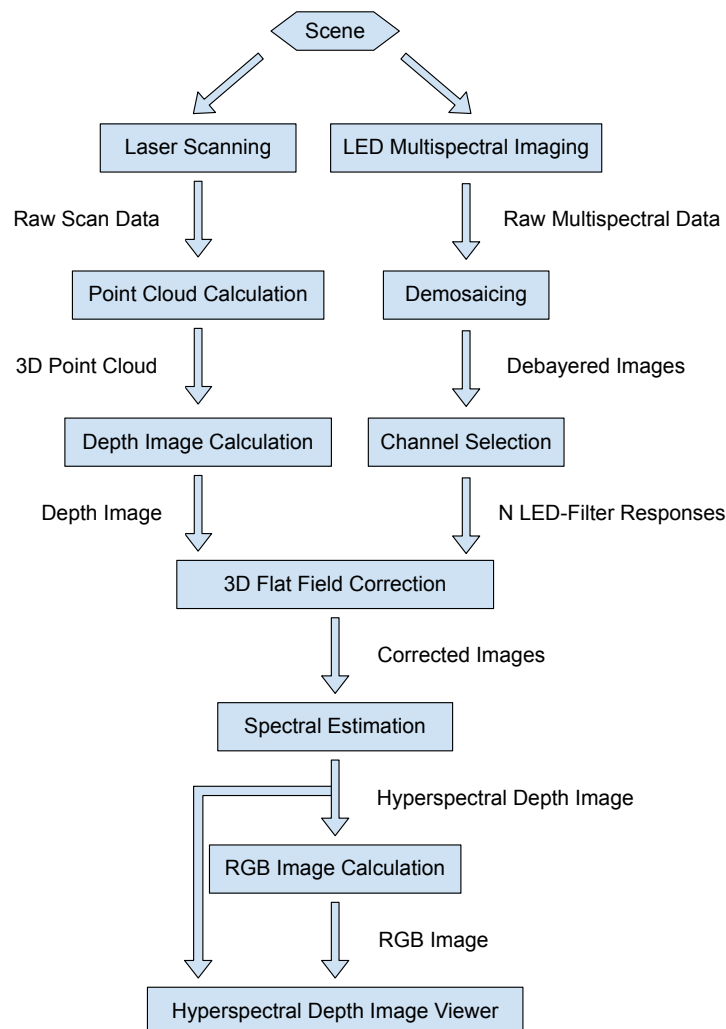because the point cloud has sub-pixel resolution and the depth image has the same resolution as the sensor. The depth image simply contains the distance from the scene point to the camera plane. This information is needed for the 3D Flat Field Correction.

LED Multispectral Imaging: Multispectral area scanning is performed with the developed light source by illuminating the scene with the light of K different narrow band LEDs. The raw multispectral data consists of the camera images. One for each LED-channel. The raw images contain a Bayer-mosaic because of the RGB camera sensor.

Demosaicing: A demosaicing step was added to sustain the resolution of the depth image. The method of choice for this was bilinear demosaicing, which simply averages the neighboring pixel values for one channel to calculate the missing pixel. More sophisticated methods exist, but for the integration in a multispectral imaging system, further research might be needed. The output of this process are K RGB images which are equivalent to $N = 3K$ LED-filter combinations.

Channel Selection: Some of the N LED-filter combinations are useless because they contain mainly noise. For example, the blue camera channel combined with a red LED results in a low signal to noise ratio. These channels are sorted out in this step to perform the spectral estimation on reasonable data.

3D Flat Field Correction: The depth information is used to correct the pixel values for spectral estimation based on a model assumption of the light distribution. A detailed description of this can be found in section 3.4. Not every pixel in the depth image contains depth information, for example, shadow areas where no laser is detectable are not known in the depth image. For these pixels, the 3D Flat Field Correction writes the value zero in the image.

Spectral Estimation: The corrected images are ready for spectral estimation. As the estimator Linear Regression was chosen based on the results of the dry experiments. Performing the estimation for every pixel results in a hyperspectral image which can be combined with the

depth image to know for every pixel its distance from the camera plane and the reflectance of the corresponding surface point.

RGB Image Calculation: From the hyperspectral image, an RGB image is calculated following the instructions from section 2.2.3.

Hyperspectral Depth Image Viewer: The RGB image and the hyperspectral depth image are passed to the Hyperspectral Depth Image Viewer which enables the analysis of the final product.

The laser scanning and the point cloud calculation processes are performed by Seavision software. All other steps result from this work and are implemented in python. For this work, the hyperspectral depth image is chosen to be the final product because it contains all the necessary information and the implementation effort is smaller than for a hyperspectral point cloud. However, the latter can still be generated from the hyperspectral depth image. In that case, the spatial sub-pixel resolution of the point can be sustained.

4.2   3D Underwater Experiment

4.2.1   Description

The 3D underwater multispectral imaging system was tested in a water tank with different targets. The first target was the ColorChecker board. It was also needed to train the Linear Regression spectral estimation method. The target was imaged twice: Once flat and once with an angle of 55 degrees to the bottom. Another imaged target scene was closer to a real-world scene. It contained several aquaristic plants and artificial plants out of polymers which are usually hard to distinguish with conventional imaging. For this experiment, the LED light source was mounted close to the camera of one Seavision unit, because only one camera was used. The tank had a maximum depth of 1 meter and for calibration, a white board was placed at its bottom. The system was looking down on it. For the calibration, 6 images of the calibration board were taken in 5 cm steps, starting at a distance of 70 cm. The calibration model was not changed for underwater calibration and it fitted the data well. The average MAPE over all channels for the calibration is 0.0207, which is better than the results presented in section 3.4.2. The smaller calibration error might be explained by improved experimental conditions. The translation of the system for the calibration was done with precisely 3D printed blocks. Consequently, there are no errors introduced by different tilt angles of the system during calibration data acquisition. Also, the target's surface quality is more consistent than the before used white wall. This also contributes to the better data. Additionally, the distances were relatively small and consequently, the effects of water attenuation are not strong for most wavelengths. However, for the 727 nm LED-channel the

attenuation was already very significant. All images were done with the same camera exposure of 8 ms, which led to no usable data from that channel.

4.2.2 Results

The Linear Regression underwater resulted in higher error than in the dry evaluation. A slightly larger error was expected because of the missing near-infrared channel. But instead of measuring a MAPE around 10 percent, it rose to 17,8 percent. The RMSE increased to a value of 0.0428. The largest influence on that had the white patch. This can be seen in the spectral estimations shown in figure 4.3. The largest error was observed on the white patch, number 19. The other patches only showed a slight increase of the error, see patch 15 and 16 in figure 4.3.
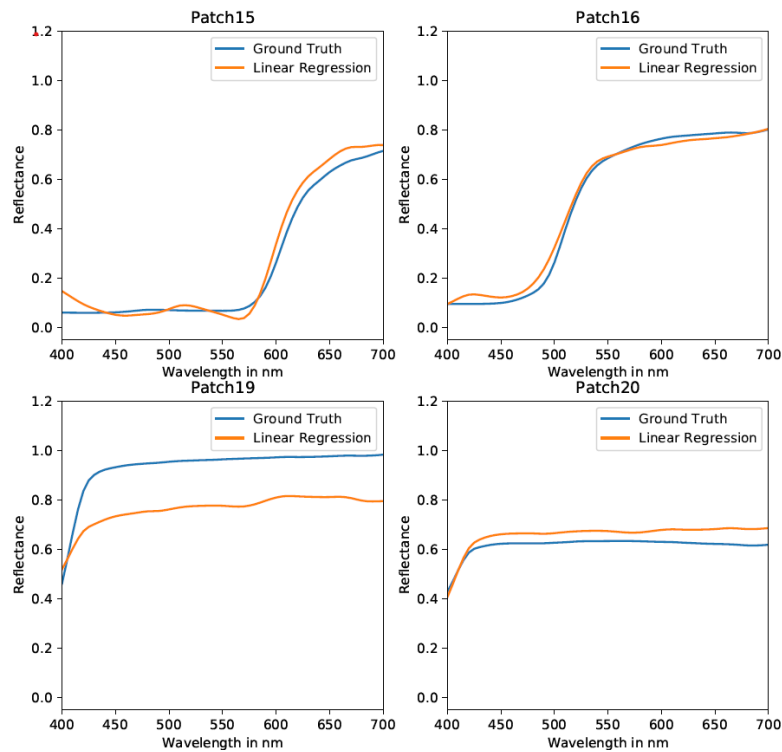
Figure 4.3: Underwater spectral estimation and ground truth data.

The large error led to the assumption that the contact with water changes the light-matter interaction and thus the ColorChecker's reflectance. This makes the dry measured ground truth data invalid for the underwater regression model fitting. Figure 4.4 shows a picture of this effect. The ColorChecker board was photographed in air and in 10 mm of water. Clearly, both patches became darker in water. This might also have been reasoned in some incident light being reflected from the water surface. Some specular reflectance can even be seen in the bottom-right corner of the figure. The important issue is, that not every patch became darker by the same amount.
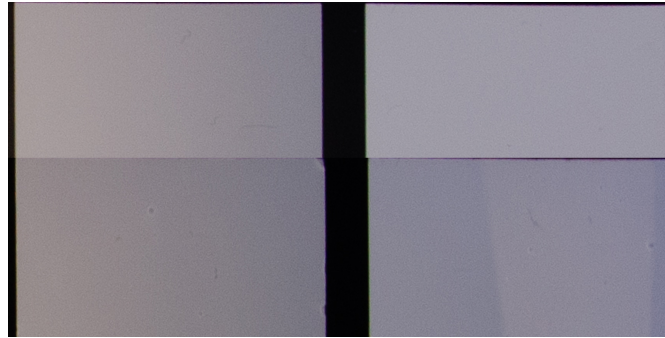
Figure 4.4: Picture of the ColorChecker patch 19 and 20. Top half is in air and bottom half is covered by 10 mm of water. Right: Patch 19. Left: Patch 20. Camera: Nikon D7000

In the dry, patch 19 was easier to distinguish from patch 20, than in the water. This subjective impression is supported by a second measurement with the Seavision camera whose linearity was shown. An analysis of the pixel brightness values from ColorChecker pictures in water and in air showed a change of relative brightness between patches 19 and 20. In air patch 20 reached 70.9 percent of the white patch's brightness and in water, this value rose to 80.7 percent. Consequently, patch 19 became darker by a higher amount, which influenced the training of the Linear Regression. Moreover, the error calculations lost their expressiveness. Therefore, the use of a dry trained regression or the Wiener Estimation would also not have led to useful validation data. Although a quantitative system validation was not possible with this data, the larger error did not significantly influence the following, qualitative analysis of the experiment results.

The RGB presentation of the scene can be obtained in two manners. One was described above and uses the hyperspectral depth image. The other way is to generate a hyperspectral image by attempting all pixels are in the same plane and calculate the RGB colors from that. The second way might be useful when the point cloud is not dense enough to give an accurate impression of the scene. Figure 4.5 shows these 3 representations for the angled ColorChecker board and the plant target. The depth image RGB for the plant target did contain many black pixels which stand for no depth information at that point. This was caused by the small features in the scene which were challenging for the structured light system.

However, the depth measurement provided critical information for the spectral estimation as the average measurements for patch 5 of the angled target in figure 4.6 show. The fixed distance hyperspectral image assumed z=950 mm for every pixel. This was simulating a conventional 2D spectral imaging system. The estimations from the hyperspectral depth image were significantly closer to the two ground truth spectra. For reference, both the 15-degree training data and the 75-degree measurement are presented. Except for indirect angle influence compensation during the Flat Field Correction, no further correction of this was done. The spectrophotometer measurements showed that for the ColorChecker board, this would be a difficult task because the
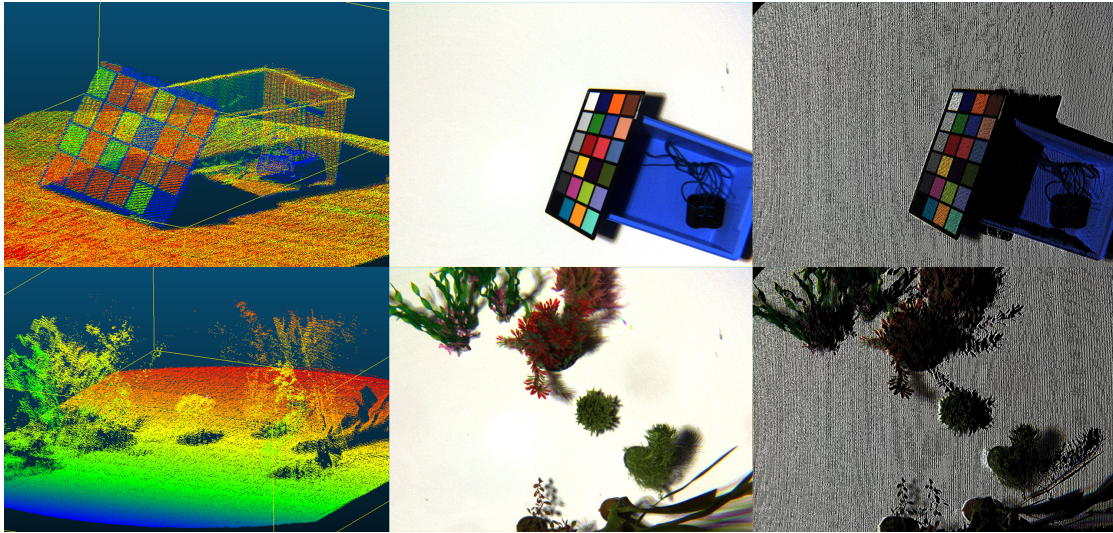
Figure 4.5: Top: Angled ColorChecker target. Bottom: Plant target. Left: 3D point clouds. Middle: Fixed distance RGB calculations. Right: Depth image RGB calculations.
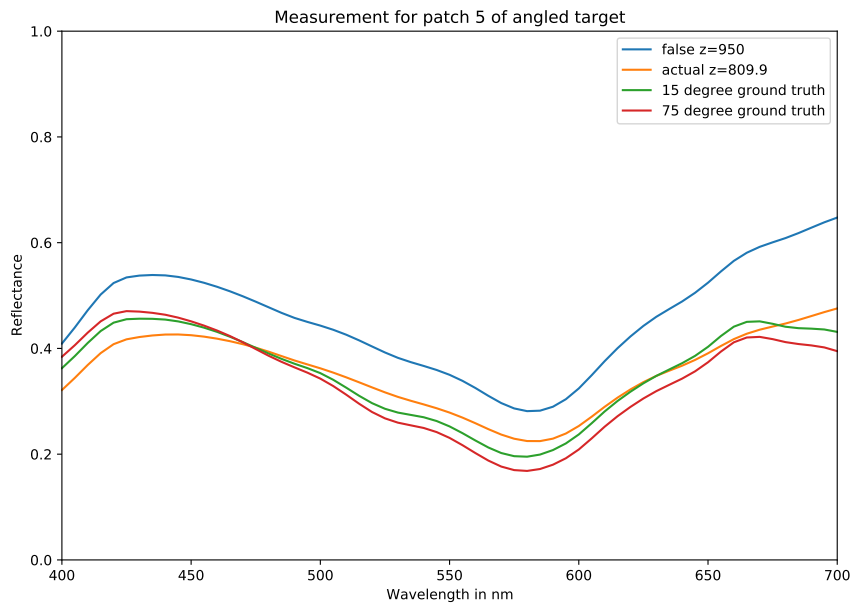
Figure 4.6: Effect of the distance information on the measured spectrum of patch 5 on the angled target. Ground truth data for a 15 and 75 degree measurement geometry is given for reference.

effect is wavelength-dependent. Even though the angle influence was not considered, the example shows the system's advantage over 2D spectral imaging systems, when the scene is not flat or the distance variable and unknown.
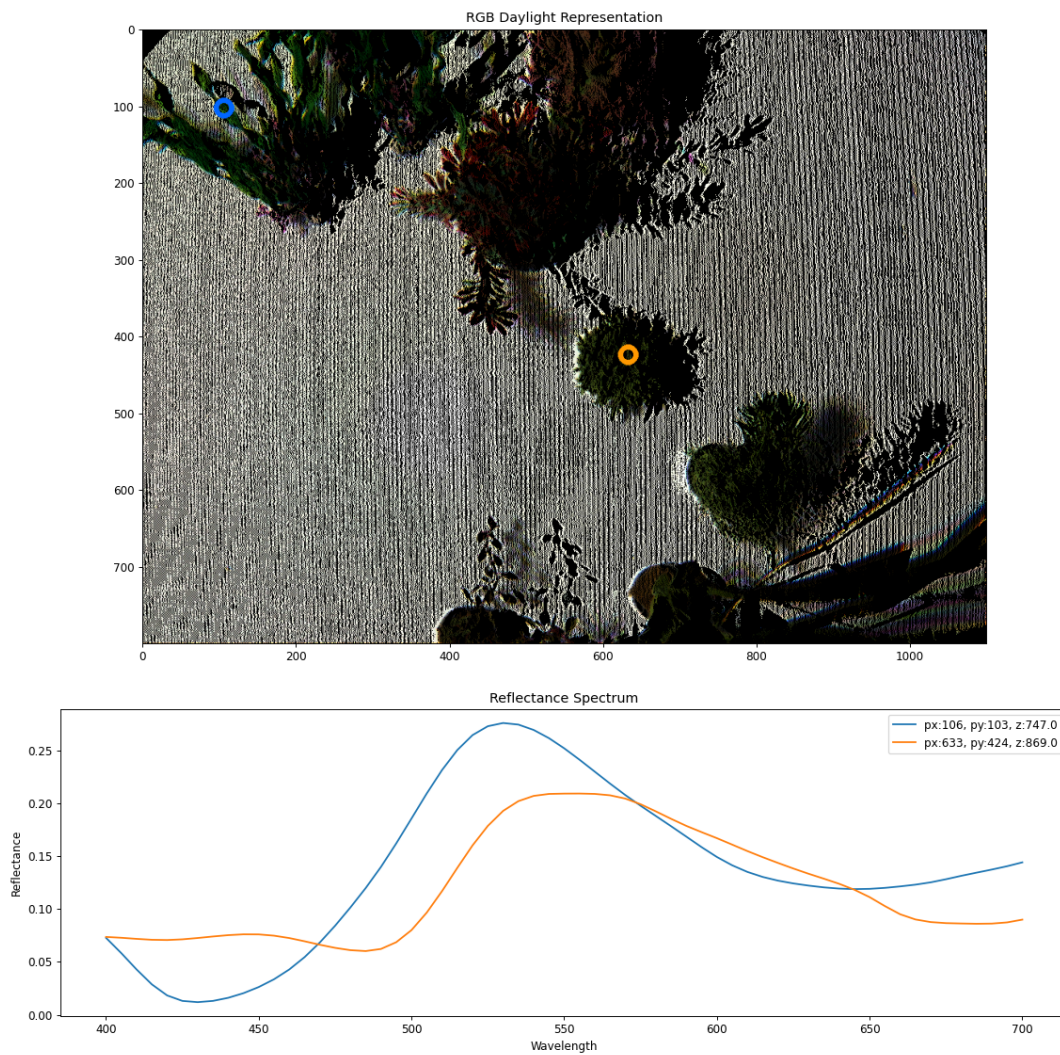
Figure 4.7: Comparison of two spectra in the hyperspectral depth image viewer from the plant target. Circles show the corresponding sample pixel location. The blue line is from an artificial plant and the orange line is from a real plant.

In the developed viewer software spectra from different pixels can be compared. Figure 4.7 shows this for the plant target. The blue sample shows the reflectance of an artificial plant surface point and the orange sample shows the spectrum of the real plant. The legend in the plot shows the pixel coordinates and the depths of the corresponding surface point. From the shown spectra, the artificial plant can be clearly distinguished from the real plant. This makes the system suitable for underwater classification tasks, which is envisaged to be a major use case for the system.

Chapter 5

Conclusion and Outlook

5.1   Thesis Summary

The objective of this work was the development of a 3D underwater LED multispectral imaging system. There is great potential in the combination of 3D and multispectral imaging because the 3D information can be used to correct scene geometry influences on the reflectance measurement. This potential increases further in underwater applications, because light absorption through water significantly influences the light's composition depending on the scene points distance. The focus on a LED-based system was motivated by the recent development of narrow-band high-power LEDs and their relatively low cost market availability. The state of the art of LED multispectral imaging was presented by this work. The shown approaches were limited to flat scenes and it was concluded that this limitation was reasoned in the Flat Field Correction that is usually only provided for a certain distance. This work proposed a method to perform a Flat Field Correction on a 3-dimensional scene by modeling the light distribution with Gaussian distribution functions. After this preprocessing the multispectral data can be used for spectral estimation, which is calculating a hyperspectral image from multispectral data. The fundamentals for this were given with the derivation of the LED multispectral image acquisition model and an introduction to different spectral estimation methods. After the theoretical foundation was given, a concept for an underwater multispectral imaging LED light source was presented. Developing from this concept was an interdisciplinary task including the design of 2 PCBs, a pressure housing, and software for microcontroller operation. This light source can build a multispectral imaging system with any camera. It was used to validate the proposed 3D Flat Field Correction model. The combination of the light source, camera and calibration already formed a multispectral imaging system. However, spectral estimation methods were applied to data acquired by that system. All introduced methods showed reasonable results. It was possible to generate a system model for a successful Wiener Estimation from datasheet values. The best performance on the test data was achieved by Linear Regression. Therefore, this method was used to calculate a hyperspectral depth image in the final system integration. The LED light source was combined with the camera of an underwater structured light system to form the objective of this thesis. In a first underwater experiment, it was shown that this prototype has advantages over classical 2D approaches and that it can support underwater in situ classification tasks.

5.2   Further Work

The underwater experiment showed that the used color target changed its reflectance. Even though there is no theoretical reason for worse performance in water than in air, this made a quantitative validation of the final system difficult. Future work should be based on a target with known reflectance underwater. This could still be the same target, but protected. This would possibly

make a new spectral reflectance ground truth measurement necessary, which can be seen as a chance to enhance the ground truth spectral range to the actual capabilities of the multispectral imaging system. Another improvement in the future can be done with the Flat Field Correction target. It should be as large as possible and have a known, mostly constant spectral reflectance. This would, maybe, put the Wiener Estimation in favor for spectral estimation because it only needs one known reflectance target to be calibrated. Flat Field Correction and spectral estimation method calibration could thus be fused to one step.

The developed system provides the hardware interface for camera and light source synchronization to enable high-speed multispectral imaging. However, a software implementation has yet to be done and would be useful for non-static scenes. In the process of doing so, the system needs to be tested thermally, to reach the maximal light intensity from the LEDs, which have been driven very carefully up to this point.

A larger calibration target and brighter LEDs are then the basis for tests with larger distances. For the relatively small tank, the Flat Field Correction model was able to compensate for the effects of water attenuation. It has to be shown if this holds for larger distances as well.

Finally, further work should incorporate full use of the combination of 3D and spectral information from the scene. Measuring reflectances of the same scene point at different distances in something else than clear water will give useful information about additional contributions to the absorption coefficient. Furthermore, a more complex model that accurately incorporates the relative position of the camera and light source can be used to apply spectral bidirectional reflectance distribution functions to provide a more accurate reflectance estimation based on information about the scene's surface normals.

In conclusion, this thesis provides the starting point and a functional wet testing setup for a 3D LED multispectral imaging system with exciting applications in the field of underwater research and industry.

Bibliography

[1] N. Akhtar and A. Mian. Hyperspectral recovery from rgb images using gaussian processes. *IEEE Transactions on Pattern Analysis and Machine Intelligence*, page 0, 10 2018.

[2] J. M. Amigo. Chapter 1.1 - hyperspectral and multispectral imaging: setting the scene. In J. M. Amigo, editor, *Hyperspectral Imaging*, volume 32 of *Data Handling in Science and Technology*, pages 3 – 16. Elsevier, 2020.

[3] J. M. Amigo and S. Grassi. Chapter 1.2 - configuration of hyperspectral and multispectral imaging systems. In J. M. Amigo, editor, *Hyperspectral Imaging*, volume 32 of *Data Handling in Science and Technology*, pages 17 – 34. Elsevier, 2020.

[4] Blue Robotics Inc. Under pressure. https://bluerobotics.com/learn/under-pressure/, 2020. Version 4.60.

[5] F. J. Burgos, M. Vilaseca, E. Perales, J. A. Herrera-Ramírez, F. M. Martínez-Verdú, and J. Pujol. Spectral led-based tuneable light source for the reconstruction of cie standard illuminants. In A. Elmoataz, O. Lezoray, F. Nouboud, and D. Mammass, editors, *Image and Signal Processing*, pages 115–123, Cham, 2014. Springer International Publishing.

[6] C. E. Rasmussen and C. K. I. Williams. *Gaussian Processes for Machine Learning*. The MIT Press, London, 2006.

[7] Computational Spectral Imaging Group, University of Eastern Finland. Munsell colors matt (Spectrofotometer measured). https://sites.uef.fi/spectral/munsell-colors-matt-spectrofotometer-measured/. [Online; accessed 30-3-2021].

[8] A. Duda. *Underwater Visual Multi-Modal 3D Sensing*. 2020.

[9] G. ElMasry and D.-W. Sun. Chapter 1 - principles of hyperspectral imaging technology. In D.-W. Sun, editor, *Hyperspectral Imaging for Food Quality Analysis and Control*, pages 3 – 43. Academic Press, San Diego, 2010.

[10] ERIKS. O-Ring Calculator. https://oringcalculator.eriksgroup.com/, 2020. [Online; accessed 12-6-2020].

[11] FRAMOS. *Sony IMX290LLR / IMX290LQR Sensor Module*, 2020. v1.1b.

[12] L. Giannoni, F. Lange, and I. Tachtsidis. Hyperspectral imaging solutions for brain tissue metabolic and hemodynamic monitoring: Past, current and future developments. *Journal of Optics*, 20:044009, 03 2018.

[13] H. Haneishi, T. Hasegawa, A. Hosoi, Y. Yokoyama, N. Tsumura, and Y. Miyake. System design for accurately estimating the spectral reflectance of art paintings. *Appl. Opt.*, 39(35):6621–6632, Dec 2000.

[14] J. Y. Hardeberg. *Acquisition and reproduction of color images: colorimetric and multispectral approaches*. Universal-Publishers, 2001.

[15] V. Heikkinen. Spectral reflectance estimation using gaussian processes and combination kernels. *IEEE Transactions on Image Processing*, 27(7):3358–3373, 2018.

[16] V. Heikkinen, R. Lenz, T. Jetsu, J. Parkkinen, M. Hauta-Kasari, and T. Jääskeläinen. Evaluation and unification of some methods for estimating reflectance spectra from rgb images. *J. Opt. Soc. Am. A*, 25(10):2444–2458, Oct 2008.

[17] J. Herrera-Ramírez, M. Vilaseca, and J. Pujol. Portable multispectral imaging system based on light-emitting diodes for spectral recovery from 370 to 1630 nm. *Appl. Opt.*, 53(14):3131–3141, May 2014.

[18] H. Holden and E. LeDrew. Hyperspectral discrimination of healthy versus stressed corals using in situ reflectance. *Journal of Coastal Research*, 17:0, 09 2001.

[19] J. B. IV, H. Blasinski, and J. Farrell. The color of water: using underwater photography to estimatewater quality. In N. Sampat, R. Tezaur, S. Battiato, and B. A. Fowler, editors, *Digital Photography X*, volume 9023, pages 224 – 234. International Society for Optics and Photonics, SPIE, 2014.

[20] KiCad Developers Team. KiCad. https://kicad.org/, 2019. Version (5.1.5)-3.

[21] S. J. Koppal. *Lambertian Reflectance*, pages 441–443. Springer US, Boston, MA, 2014.

[22] H. Liang. Liang, h. advances in multispectral and hyperspectral imaging for archaeology and art conservation. applied physics a: Materials science and processing. *Applied Physics A*, 106, 02 2011.

[23] H. Liu, J. Sticklus, K. Köser, H.-J. T. Hoving, H. Song, Y. Chen, J. Greinert, and T. Schoening. Tulumis - a tunable led-based underwater multispectral imaging system. *Opt. Express*, 26(6):7811–7828, Mar 2018.

[24] E. McHugh, J. Girard, L. Denes, P. Metes, and C. Sabine. Current research on slope movement in mines: Use of hyperspectral imagery. 05 2021.

[25] P. Mishra, G. Polder, and N. Vilfan. Close range spectral imaging for disease detection in plants using autonomous platforms: a review on recent studies. *Current Robotics Reports*, 1:43–48, June 2020.

[26] M. Parmar, S. Lansel, and J. Farrell. An led-based lighting system for acquiring multispectral scenes. *Proceedings of SPIE - The International Society for Optical Engineering*, 8299:23–, 01 2012.

[27] F. Pedregosa, G. Varoquaux, A. Gramfort, V. Michel, B. Thirion, O. Grisel, M. Blondel, P. Prettenhofer, R. Weiss, V. Dubourg, J. Vanderplas, A. Passos, D. Cournapeau, M. Brucher, M. Perrot, and E. Duchesnay. Scikit-learn: Machine learning in Python. *Journal of Machine Learning Research*, 12:2825–2830, 2011.

[28] R. M. Pope and E. S. Fry. Absorption spectrum (380–700 nm) of pure water. ii. integrating cavity measurements. *Appl. Opt.*, 36(33):8710–8723, Nov 1997.

[29] J. Qin. Chapter 5 - hyperspectral imaging instruments. In D.-W. Sun, editor, *Hyperspectral Imaging for Food Quality Analysis and Control*, pages 129 – 172. Academic Press, San Diego, 2010.

[30] R. J. Radke. *Three-Dimensional Data Acquisition*, page 300–352. Cambridge University Press, 2012.

[31] A. Ribes and F. Schmitt. Linear inverse problems in imaging. *IEEE Signal Processing Magazine*, 25(4):84–99, 2008.

[32] R.W.G. Hunt and M.R. Pointer. Colour vision. In *Measuring Colour*, chapter 1, pages 1–17. John Wiley and Sons, Ltd, 07 2011.

[33] R.W.G. Hunt and M.R. Pointer. Obtaining spectral data and tristimulus values. In *Measuring Colour*, chapter 5, pages 99–115. John Wiley and Sons, Ltd, 07 2011.

[34] M. Sasano, M. Imasato, H. Yamano, and H. Oguma. Development of a regional coral observation method by a fluorescence imaging lidar installed in a towable buoy. *Remote Sensing*, 8:48, 01 2016.

[35] R. Shrestha and J. Hardeberg. Multispectral imaging using led illumination and an rgb camera. *Color and Imaging Conference*, 01 2013.

[36] R. Shrestha and J. Hardeberg. An experimental study of fast multispectral imaging using led illumination and an rgb camera. *Color and Imaging Conference*, 2015, 10 2015.

[37] J. Tschannerl, J. Ren, H. Zhao, F.-J. Kao, S. Marshall, and P. Yuen. Hyperspectral image reconstruction using multi-colour and time-multiplexed led illumination. *Optics and Lasers in Engineering*, 121:352–357, 10 2019.

[38] P. Virtanen, R. Gommers, T. E. Oliphant, M. Haberland, T. Reddy, D. Cournapeau, E. Burovski, P. Peterson, W. Weckesser, J. Bright, S. J. van der Walt, M. Brett, J. Wilson, K. J. Millman, N. Mayorov, A. R. J. Nelson, E. Jones, R. Kern, E. Larson, C. J. Carey, İ. Polat, Y. Feng, E. W. Moore, J. VanderPlas, D. Laxalde, J. Perktold, R. Cimrman, I. Henriksen, E. A. Quintero, C. R. Harris, A. M. Archibald, A. H. Ribeiro, F. Pedregosa, P. van Mulbregt, and SciPy 1.0 Contributors. SciPy 1.0: Fundamental Algorithms for Scientific Computing in Python. *Nature Methods*, 17:261–272, 2020.

[39] H. Wang, Y. Hu, X. Ma, J. Sun, X. Sun, D. Chen, X. Zheng, and Q. Li. An active hyperspectral imaging system based on a multi-led light source. *Review of Scientific Instruments*, 90(2):026107, 2019.

[40] Wikipedia. Spline-interpolation — wikipedia, die freie enzyklopaedie. https://de.wikipedia.org/w/index.php?title=Spline-Interpolation&oldid=207936348, 2021. [Online; Stand 19. April 2021].

[41] Wikipedia contributors. Cie 1931 color space — Wikipedia, the free encyclopedia. https://en.wikipedia.org/w/index.php?title=CIE_1931_color_space&oldid=1012855413, 2021. [Online; accessed 9-April-2021].

[42] Wikipedia contributors. False color — Wikipedia, the free encyclopedia. https://en.wikipedia.org/w/index.php?title=False_color&oldid=1011887157, 2021. [Online; accessed 9-April-2021].

[43] Wikipedia contributors. Illuminant d65 — Wikipedia, the free encyclopedia. https://en.wikipedia.org/w/index.php?title=Illuminant_D65&oldid=1000730682, 2021. [Online; accessed 9-April-2021].

[44] Wikipedia contributors. Mean absolute error — Wikipedia, the free encyclopedia. https://en.wikipedia.org/w/index.php?title=Mean_absolute_error&oldid=1006570292, 2021. [Online; accessed 22-April-2021].

[45] Wikipedia contributors. Mean absolute percentage error — Wikipedia, the free encyclopedia. https://en.wikipedia.org/w/index.php?title=Mean_absolute_percentage_error&oldid=1014081808, 2021. [Online; accessed 6-April-2021].

[46] Wikipedia contributors. Regression analysis — Wikipedia, the free encyclopedia. https://en.wikipedia.org/w/index.php?title=Regression_analysis&oldid=1018847859, 2021. [Online; accessed 20-April-2021].

[47] Wikipedia contributors. Root-mean-square deviation — Wikipedia, the free encyclopedia. https://en.wikipedia.org/w/index.php?title=Root-mean-square_deviation&oldid=1006091401, 2021. [Online; accessed 6-April-2021].

[48] I. X-Rite. ColorChecker Classic. https://www.xrite.com/de/categories/calibration-profiling/colorchecker-classic. [Online; accessed 19-3-2021].

[49] I. X-Rite. New color specifications for ColorChecker SG and Classic Charts. https://www.xrite.com/de/service-support/new_color_specifications_for_colorchecker_sg_and_classic_charts. [Online; accessed 19-3-2021].

[50] H. Yao and D. Lewis. Chapter 2 - spectral preprocessing and calibration techniques. In D.-W. Sun, editor, *Hyperspectral Imaging for Food Quality Analysis and Control*, pages 45–78. Academic Press, San Diego, 2010.

Appendix

This appendix contains vector graphics optimized for the digital view. The content is not numbered, but ordered to the following index.

Contents

Connection to Driver board

J1
Conn_02x09_Row_Letter_First

GND	a1	b1	590_in
385A_in	a2	b2	615_in
385B_in	a3	b3	625_in
415_in	a4	b4	633_in
455_in	a5	b5	660A_in
470_in	a6	b6	660B_in
505_in	a7	b7	730A_in
530_in	a8	b8	730B_in
568_in	a9	b9	GND

J2
Conn_02x09_Row_Letter_First

GND	a1	b1	590_out
385A_out	a2	b2	615_out
385B_out	a3	b3	625_out
415_out	a4	b4	633_out
455_out	a5	b5	660A_out
470_out	a6	b6	660B_out
505_out	a7	b7	730A_out
530_out	a8	b8	730B_out
568_out	a9	b9	GND
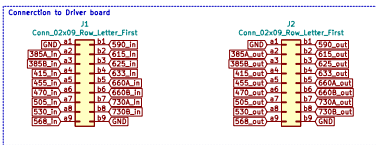
H1 MountingHole
H2 MountingHole
H3 MountingHole
H4 MountingHole

Driver 1

LED1_1 LED1_2 LED1_3 LED1_4 LED1_5 LED1_6   385A_in ... 385A_out
LED1_7 LED1_8 LED1_9 LED1_10 LED1_11   385B_in ... 385B_out

LED13_1 LED13_2 LED13_3 LED13_4 LED13_5 LED13_6 LED13_7 LED13_8 LED13_9   730A_in ... 730A_out
Thermal GND

LED13_10 LED13_11 LED13_12 LED13_13 LED13_14 LED13_15 LED13_16 LED13_17   730B_in ... 730B_out
Thermal GND

Driver 2

LED2_1 LED2_2 LED2_3 LED2_4   415_in ... 415_out
LED3_1 LED3_2 LED3_3   455_in ... 455_out
Thermal GND

LED4_1 LED4_2 LED4_3   470_in ... 470_out
LED5_1 LED5_2 LED5_3 LED5_4 LED5_5 LED5_6   505_in ... 505_out
Thermal GND

Driver 3

LED6_1 LED6_2 LED6_3 LED6_4 LED6_5 LED6_6 LED6_7 LED6_8 LED6_9   530_in ... 530_out
LED7_1 LED7_2 LED7_3 LED7_4 LED7_5 LED7_6   568_in ... 568_out
GND

LED8_1 LED8_2 LED8_3 LED8_4 LED8_5 LED8_6 LED8_7 LED8_8 LED8_9 LED8_10
LZ1-00A102
590_in ... 590_out
590_in ... 590_out
Thermal GND

LED9_1 LED9_2 LED9_3 LED9_4 LED9_5 LED9_6 LED9_7 LED9_8 LED9_9 LED9_10   615_in ... 615_out
GND

Driver 4

LED10_1 LED10_2 LED10_3 LED10_4 LED10_5 LED10_6 LED10_7   625_in ... 625_out
LED11_1 LED11_2 LED11_3 LED11_4 LED11_5 LED11_6 LED11_7 LED11_8 LED11_9 LED11_10   633_in ... 633_out
Thermal GND

LED12_1 LED12_2 LED12_3 LED12_4 LED12_5 LED12_6 LED12_7   660A_in ... 660A_out
LED12_8 LED12_9 LED12_10 LED12_11 LED12_12 LED12_13 LED12_14   660B_in ... 660B_out
Thermal GND